

TAX-Pose: Task-Specific Cross-Pose Estimation for Robot Manipulation

Chuer Pan*, Brian Okorn*, Harry Zhang*, Ben Eisner*, David Held

Robotics Institute, School of Computer Science

Carnegie Mellon University, United States

{chuerp, bokorn, haolunz, baeisner, dheld}@andrew.cmu.edu

Abstract: How do we imbue robots with the ability to efficiently manipulate unseen objects and transfer relevant skills based on demonstrations? End-to-end learning methods often fail to generalize to novel objects or unseen configurations. Instead, we focus on the task-specific pose relationship between relevant parts of interacting objects. We conjecture that this relationship is a generalizable notion of a manipulation task that can transfer to new objects in the same category; examples include the relationship between the pose of a pan relative to an oven or the pose of a mug relative to a mug rack. We call this task-specific pose relationship “cross-pose” and provide a mathematical definition of this concept. We propose a vision-based system that learns to estimate the cross-pose between two objects for a given manipulation task using learned cross-object correspondences. The estimated cross-pose is then used to guide a downstream motion planner to manipulate the objects into the desired pose relationship (placing a pan into the oven or the mug onto the mug rack). We demonstrate our method’s capability to generalize to unseen objects, in some cases after training on only 10 demonstrations in the real world. Results show that our system achieves state-of-the-art performance in both simulated and real-world experiments across a number of tasks. Supplementary information and videos can be found on our [project website](#).

Keywords: Learning from Demonstration, Manipulation, 3D Learning

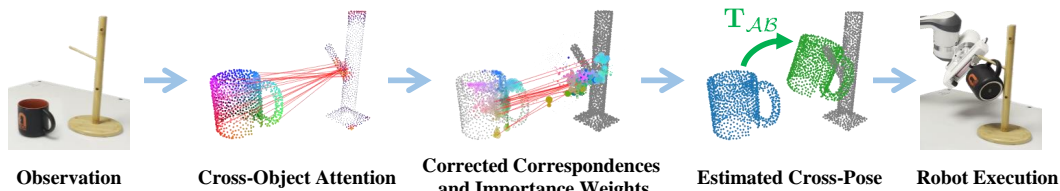


Figure 1: To solve a relative placement task, TAX-Pose uses cross-object attention to estimate dense cross-object correspondences and importance weights for each object point. This dense estimate is mapped to a single “cross-pose” which the robot uses to accomplish the given task.

1 Introduction

Many manipulation tasks require a robot to move an object to a location relative to another object. For example, a cooking robot may need to place a lasagna in an oven, place a pot on a stove, place a plate in a microwave, place a mug onto a mug rack, or place a cup onto a shelf. Understanding and placing objects in task-specific locations is a key skill for robots operating in human environments. Further, this skill should generalize to novel objects within the training categories, such as placing new trays into the oven or new mugs onto a mug rack. A common approach in robot learning is to

*Equal Contribution. See Appendix H for a detailed list of each author’s contributions.

train a policy “end-to-end,” mapping from pixel observations to low-level robot actions. However, end-to-end trained policies cannot easily reason about complex pose relationships such as the ones described above, and they have difficulty generalizing to unseen object configurations.

In contrast, we propose a method that learns to reason about the 3D geometric relationship between a pair of objects. For the type of tasks defined above, the robot needs to reason about the relationship between key parts on one object with respect to key parts on another object. For example, to place a mug on a mug rack, the robot must reason about the relationship between the pose of the mug handle and the pose of the mug rack; if the mug rack changes its pose, then the pose of the mug must change accordingly in order to still be placed on the rack (see Figure 3). We name this task-specific notion of the pose relationship between a pair of objects as “cross-pose” and we formally define it mathematically. Further, we propose a vision system that can efficiently estimate the cross-pose from a small number of demonstrations of a given task, generalizing to novel objects within the training categories. To complete the manipulation task, we use the estimated cross-pose as the target of a motion planning algorithm, which will move the objects into the desired configuration (e.g. placing the mug onto the rack, placing the lasagna into the oven, etc).

In this paper, we present TAX-Pose (TASk-specific Cross-Pose), a deep 3D vision-based method that learns to predict a task-specific pose relationship between a pair of objects from a set of demonstrations. Our cross-pose estimation system is provably translation equivariant and can generalize from a small number of real-world demonstrations (in some cases as few as 10) to new objects in unseen poses.

The contributions of this paper include:

1. A precise definition of “cross-pose,” which defines a task-specific pose relationship between two objects.
2. A novel method that estimates soft-correspondences between two objects, from which the cross-pose between the objects can be estimated (see Figure 1); this method is provably translation equivariant and can learn from a small number of real-world demonstrations.
3. A robot system to manipulate objects into the desired cross-pose to achieve a given manipulation task.

We present simulated and real-world experiments to test the performance of our system in achieving a variety of relative placement manipulation tasks. We demonstrate our method on a semantic placement task, in which the robot must place an object in, on, or around a novel object (Figure 2, top). We also demonstrate our method on precise placement tasks, such as hanging a mug on a rack (Figure 2, bottom) or placing a bottle or bowl on a shelf; in both cases our method generalizes to new object configurations and new objects within the training categories.

2 Related Work

Object Pose Estimation: Pose estimation is the task of detecting and inferring the 6DoF pose of an object, which includes its position and orientation, with respect to some previously defined object reference frame [1, 2, 3, 4, 5, 6]. Recent work [7, 8, 9, 10, 11] proposed to use 3D semantic keypoints as an alternative form of object representation. While keypoint-based methods can generalize within an object class, they require a significant amount of hand annotated data or access to a simulated

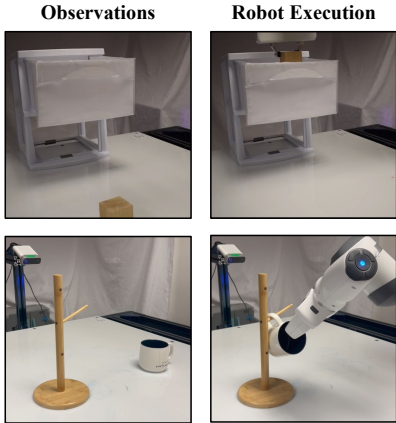


Figure 2: We study relative placement tasks, in which one object needs to be placed in a position relative to another object. Here are two of the tasks that we demonstrate our method on: **Top:** *PartNet-Mobility Placement Task* requires one object (e.g. a block) to be placed relative to another object (e.g. a drawer) by a semantic goal position (e.g. inside); **Bottom:** *Mug Hanging Task* requires placing the mug’s handle on the mug rack.

version of the task to learn to estimate the keypoint locations. In contrast, our method is able to learn from just 10 real-world demonstrations. Another approach is to use dense embeddings, such as Dense Object Nets (DON) [12, 13] and Neural Descriptor Fields (NDF) [14, 15], which achieve generalization across classes by predicting dense embeddings in the observation and matching them to embeddings of the demonstration objects. However, DON [12, 16] and NDF [14, 17] assume that the target object is moved relative to a static reference object in a “known canonical configuration” (e.g. the pose of the mug rack in NDF [14] is assumed to be known and fixed). In contrast, our method reasons about the geometric relationship between a pair of objects and hence does not need to assume a static environment. Thus, for example, our method is able to perform the mug hanging task while varying the pose of the mug rack (see our [project website](#)), whereas the baselines (DON [12], NDF [14]) cannot. Further, we show that our method significantly outperforms both the DON [12] and NDF [14] baselines, especially when given a very small number of demonstrations.

Point Cloud Registration: Our method for estimating the cross-pose between two objects builds upon previous work in point cloud registration. The typical objective in point cloud registration is to find the optimal rigid alignment between two point clouds, to minimize the sum of squared distances between two sets of points. Traditionally, Iterative Closest Point (ICP) [18, 19] and its variants [20, 21, 22, 23, 24, 25] have been used to compute the optimal rigid alignment between two point clouds. Deep Closest Point (DCP) [26] avoids local minima common for ICP by seeking to approximate correspondence in a high-dimensional learned feature space. Our method builds upon the architecture of DCP for cross-pose estimation; however, in contrast to point cloud registration, in which the objective is to minimize the sum of squared distances between two sets of points on the same object in two different poses, our objective is to estimate a task-specific pose relationship between two different objects. Extending the framework from DCP, we learn a residual to the soft correspondences, allowing for points to match outside the convex hull of each object. This component is necessary when computing soft correspondences between objects of drastically different morphologies (such as a mug and a mug rack).

3 Problem Statement

Relative placement tasks: In this paper, we are specifically interested in “relative placement tasks.” Given two objects, \mathcal{A} and \mathcal{B} , a “relative placement task” is the task of placing object \mathcal{A} at a pose relative to object \mathcal{B} . For example, consider the task of placing a lasagna in an oven, placing a mug on a rack, or placing a robot gripper on the rim of a mug. All of these tasks involve placing one object (which we call the “action” object \mathcal{A}) at a semantically meaningful location relative to another object (which we call the “anchor” object \mathcal{B})².

Specifically, suppose that \mathbf{T}_A^* and \mathbf{T}_B^* are $SE(3)$ poses for objects \mathcal{A} and \mathcal{B} respectively (in a shared world reference frame³) for which a desired task is considered complete (lasagna is in the oven; mug is on the rack, etc). Then for a relative placement task, if objects \mathcal{A} and \mathcal{B} are in poses $\mathbf{T} \cdot \mathbf{T}_A^*$ and $\mathbf{T} \cdot \mathbf{T}_B^*$ (respectively) for any transform \mathbf{T} , then the task will also be considered to be complete, as seen in Figure 3. In other words, if \mathbf{T}_B^* represents the pose of the rack and \mathbf{T}_A^* represents the pose of the mug on the rack (at task completion); then if we transform the both the mug and rack poses by \mathbf{T} , then the mug will still be

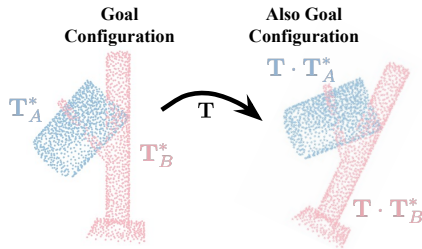


Figure 3: If we transform both the action object (mug) and the anchor object (rack) by the same transform, then the relative pose between these objects is unchanged (the mug is still “on” the rack) so the mug is still in the goal configuration.

²Note that the definition of action and anchor is symmetric; either object can be treated as the action object and the other as the anchor.

³All $SE(3)$ transformations in this work are defined in a fixed, arbitrary world frame.

located on the rack. Formally, this property can be defined with the following Boolean function,

$$\text{RelPlace}(\mathbf{T}_A, \mathbf{T}_B) = \text{SUCCESS} \text{ iff } \exists \mathbf{T} \in SE(3) \text{ s.t. } \mathbf{T}_A = \mathbf{T} \cdot \mathbf{T}_A^* \text{ and } \mathbf{T}_B = \mathbf{T} \cdot \mathbf{T}_B^*. \quad (1)$$

For many real semantic placement tasks, there are actually sets of valid solutions which solve each task (i.e., there are many potential locations to place an object on a table to achieve a semantic “object-on-table” relationship). However, for this work, we consider precise placement tasks under the simplifying assumption that, for a given pose of object \mathcal{B} , there is a single, unambiguous pose of object \mathcal{A} needed to achieve the task.

Definition of Cross-Pose: Given the above definition of a relative placement task, our goal will be to determine how to move object \mathcal{A} so that it will be in the “goal pose,” which, as described above, is defined relative to the pose of object \mathcal{B} . To achieve this, one option is to estimate the poses of objects \mathcal{A} and \mathcal{B} separately and then compute the transformation needed to move object \mathcal{A} into the goal pose. However, the pose estimate of each object will have errors, and these errors will accumulate when the poses are combined into the single relative pose needed to reach the goal configuration.

Instead of estimating the pose of each object independently, we aim to learn a function $f(\mathbf{P}_A, \mathbf{P}_B)$, which takes as input the point clouds \mathbf{P}_A and \mathbf{P}_B for both objects \mathcal{A} and \mathcal{B} , where $\mathbf{P}_A \in \mathbb{R}^{3 \times N_A}$ and $\mathbf{P}_B \in \mathbb{R}^{3 \times N_B}$ are 3D point clouds of sizes N_A and N_B , respectively. This function outputs an $SE(3)$ rigid transformation, $f(\mathbf{P}_A, \mathbf{P}_B) = \mathbf{T}_{AB}$, where we refer to \mathbf{T}_{AB} as the “cross-pose” between object \mathcal{A} and object \mathcal{B} . For notational convenience, we occasionally write f as a function of the poses $\mathbf{T}_A, \mathbf{T}_B$ of point clouds \mathbf{P}_A and \mathbf{P}_B respectively (with respect to a global reference frame) such that $f(\mathbf{T}_A, \mathbf{T}_B) := f(\mathbf{P}_A, \mathbf{P}_B)$. This notational change is to make the transformation math more intuitive; in practice, this function only ever receives point clouds as input.

We will define the cross-pose \mathbf{T}_{AB} (below) such that, if we transform object \mathcal{A} by \mathbf{T}_{AB} , then object \mathcal{A} will be in the goal pose relative to object \mathcal{B} for the relative placement task. For example, suppose that \mathbf{T}_A^* and \mathbf{T}_B^* are poses for objects \mathcal{A} and \mathcal{B} , respectively, for which a desired relative placement task is considered complete. In this configuration, the cross-pose of these objects would be $f(\mathbf{T}_A^*, \mathbf{T}_B^*) = \mathbf{I}$ where \mathbf{I} is the identity, as object \mathcal{A} does not need to be moved to complete the task. Further, based on the definition of a relative placement task given above, if both objects are transformed by the same transform \mathbf{T} , then the objects will still be in the desired relative pose,

$$f(\mathbf{T} \cdot \mathbf{T}_A^*, \mathbf{T} \cdot \mathbf{T}_B^*) = f(\mathbf{T}_A^*, \mathbf{T}_B^*) = \mathbf{I} \quad (2)$$

for any transform $\mathbf{T} \in SE(3)$. Now, let us assume that objects \mathcal{A} and \mathcal{B} are not in the goal configuration and have pose $\mathbf{T}_A = \mathbf{T}_\alpha \cdot \mathbf{T}_A^*$ and $\mathbf{T}_B = \mathbf{T}_\beta \cdot \mathbf{T}_B^*$, respectively, for arbitrary transforms \mathbf{T}_α and $\mathbf{T}_\beta \in SE(3)$. We then define the “cross-pose” of objects \mathcal{A} and \mathcal{B} as:

$$f(\mathbf{T}_A, \mathbf{T}_B) = f(\mathbf{T}_\alpha \cdot \mathbf{T}_A^*, \mathbf{T}_\beta \cdot \mathbf{T}_B^*) = \mathbf{T}_{AB} := \mathbf{T}_\beta \cdot \mathbf{T}_\alpha^{-1}. \quad (3)$$

Note that this definition is equivalent to Equation 2 for the special case of $\mathbf{T}_\alpha = \mathbf{T}_\beta$. This definition of cross-pose allows us to move object \mathcal{A} into the goal configuration, relative to object \mathcal{B} :

$$\mathbf{T}_{AB} \cdot \mathbf{T}_A = (\mathbf{T}_\beta \cdot \mathbf{T}_\alpha^{-1}) \cdot (\mathbf{T}_\alpha \cdot \mathbf{T}_A^*) = \mathbf{T}_\beta \cdot \mathbf{T}_A^*, \quad (4)$$

satisfying the relative placement condition defined in Equation 1 with $\mathbf{T} = \mathbf{T}_\beta$. Alternatively, we could have instead transformed object \mathcal{B} by the inverse of the cross-pose to achieve the task.

4 Method

Overview: We frame the task of cross-pose estimation as a soft correspondence-prediction task between a pair of point clouds, followed by an analytical least-squares optimization to find the optimal *cross-pose* for the predicted correspondences. As described in Appendix B, this correspondence-based approach allows our method to be translation-equivariant: translating either object (\mathcal{A} or \mathcal{B}) will lead to a translated cross-pose prediction. This allows our method to automatically adapt to novel positions of both the anchor and action objects, unlike previous work which assumes a static anchor [14]. Our method for task-specific cross-pose estimation, known as TAX-Pose, consists of the following steps, as shown in Figure 4:

1. **Soft Correspondence Prediction:** For a pair of objects \mathcal{A}, \mathcal{B} , a neural network learns to predict a per-point embedding to establish a (soft) correspondence between \mathcal{A} and \mathcal{B} , which are called “virtual soft correspondences.” The corresponding points are constrained to be within the convex hulls of \mathcal{B} and \mathcal{A} respectively.
2. **Adjustment via Correspondence Residuals:** For most estimation tasks, some points in object \mathcal{A} may not be within the convex hull of object \mathcal{B} ; for instance, when a mug is placed on a mug rack, most points on the mug will be outside of the convex hull of the mug rack. To accommodate these cases, we apply a pointwise residual vector to displace each of the predicted soft correspondences. These “corrected virtual correspondences” allow points in \mathcal{A} to correspond to locations in free space near \mathcal{B} .
3. **Find the Optimal Transform:** Because the cross-pose is defined as a rigid transformation of object \mathcal{A} , we use a differentiable weighted SVD to find the transformation that minimizes the weighted least squares difference to the corrected virtual correspondences.

Because each step above is differentiable, the whole model can be optimized end-to-end, despite having an interpretable internal structure which we describe below. Our method is heavily inspired by Deep Closest Point (DCP) [26]. The key difference between our pose alignment model and DCP is that we predict the cross-pose between two *different* objects for a given task instead of registering two point clouds of an identical object. Additionally, TAX-Pose can predict relationships where these clouds may not have any points of contact or overlap.

We now describe our cross-pose estimation algorithm in detail. To recap the problem statement, given objects \mathcal{A} and \mathcal{B} with point cloud observations $\mathbf{P}_A \in \mathbb{R}^{3 \times N_A}$, $\mathbf{P}_B \in \mathbb{R}^{3 \times N_B}$ respectively, our objective is to estimate the task-specific cross-pose $\mathbf{T}_{AB} = f(\mathbf{P}_A, \mathbf{P}_B) \in SE(3)$. Note that the cross-pose between object \mathcal{A} and \mathcal{B} is defined with respect to a given task (e.g. putting a lasagna in the oven, putting a mug on the rack, etc).

4.1 Cross-Pose Estimation via Soft Correspondence Prediction

Soft Correspondence Prediction: The first step of the method is to compute two sets of correspondences between \mathcal{A} and \mathcal{B} , one which maps from points in \mathcal{A} to \mathcal{B} , and one which maps from points in \mathcal{B} to \mathcal{A} . These need not be a bijection, and can be asymmetric. As we want each step to be differentiable, we follow DCP’s conventions and estimate a *soft correspondence*. This assigns a *virtual soft corresponding point* $\mathbf{v}_i^A \in \mathbf{V}_A$ to every point $\mathbf{p}_i^A \in \mathbf{P}_A$ by computing a convex combination of points in \mathbf{P}_B , and vice versa. Formally:

$$\mathbf{v}_i^A = \mathbf{P}_B \mathbf{w}_i^{A \rightarrow B} \quad \text{s.t.} \quad \sum_{j=1}^{N_B} w_{ij}^{A \rightarrow B} = 1 \quad (5a) \quad \mathbf{v}_i^B = \mathbf{P}_A \mathbf{w}_i^{B \rightarrow A} \quad \text{s.t.} \quad \sum_{j=1}^{N_A} w_{ij}^{B \rightarrow A} = 1 \quad (5b)$$

with normalized weight vectors $\mathbf{w}_i^{A \rightarrow B} \in \mathbf{W}_{A \rightarrow B}$ and $\mathbf{w}_i^{B \rightarrow A} \in \mathbf{W}_{B \rightarrow A}$. Importantly, these virtual

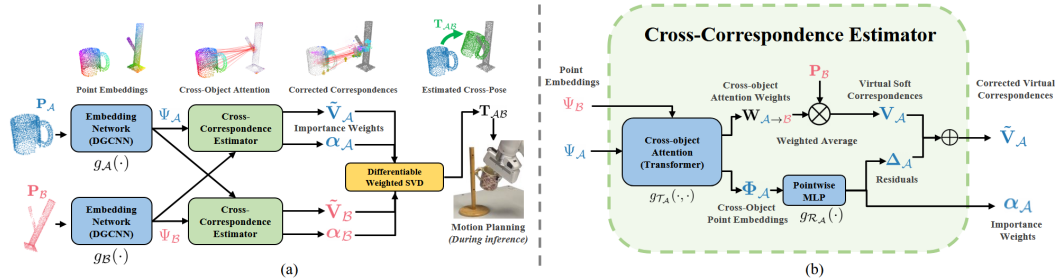


Figure 4: TAX-Pose Training Overview: Given a specific task, our method takes as input two point clouds and outputs the cross-pose between them needed to achieve the task. TAX-Pose first learns point clouds features using two DGCNN [27] networks and two Transformers [28]. Then the learned features are each input to a point residual network to predict per-point soft correspondences and weights across the two objects. The desired cross-pose can be inferred analytically from these correspondences using singular value decomposition.

corresponding points are not constrained to the surfaces of \mathcal{A} or \mathcal{B} ; instead, they are constrained to the convex hulls of \mathbf{P}_B and \mathbf{P}_A , respectively.

To compute the weights $\mathbf{w}_i^{A \rightarrow B}$, $\mathbf{w}_i^{B \rightarrow A}$ in Equations 5a and 5b, we first encode each point cloud \mathbf{P}_A and \mathbf{P}_B into a latent space using a neural network encoder, DGCNN [27]. This encoder head is comprised of two distinct encoders g_A and g_B , each of which receives point cloud \mathbf{P}_A and \mathbf{P}_B , respectively, zero-centers them, and outputs a dense, point-wise embedding for each object (see Figure 4): $\Psi_A = g_A(\bar{\mathbf{P}}_A) \in \mathbb{R}^{N_A \times d}$, $\Psi_B = g_B(\bar{\mathbf{P}}_B) \in \mathbb{R}^{N_B \times d}$ where $\psi_i^K \in \Psi_K$ is the d -dimensional embedding of the i -th point in object \mathcal{K} , and $\bar{\mathbf{P}}_K$ is the zero-centered point cloud for object \mathcal{K} . Because we want the cross-correspondence to incorporate information about both point clouds, we then employ a cross-object attention module between the two dense feature sets to obtain *cross-object point embeddings*, $\Phi_A \in \mathbb{R}^{N_A \times d}$ and $\Phi_B \in \mathbb{R}^{N_B \times d}$, defined as:

$$\Phi_A = \Psi_A + g_{\mathcal{T}_A}(\Psi_A, \Psi_B), \quad \Phi_B = \Psi_B + g_{\mathcal{T}_B}(\Psi_B, \Psi_A) \quad (6)$$

where $g_{\mathcal{T}_A}$, $g_{\mathcal{T}_B}$ are Transformers [28].

Finally, recall that our goal was to compute a set of normalized weight vectors $\mathbf{W}_{A \rightarrow B}$, $\mathbf{W}_{B \rightarrow A}$. To compute the virtual corresponding point \mathbf{v}_i^A assigned to any point $\mathbf{p}_i^A \in \mathbf{P}_A$, we can extract the desired normalized weight vector $\mathbf{w}_i^{A \rightarrow B}$ from intermediate attention features of the cross-object attention module as:

$$\mathbf{w}_i^{A \rightarrow B} = \text{softmax} \left(\frac{\mathbf{K}_B \mathbf{q}_i^A}{\sqrt{d}} \right), \quad \mathbf{w}_i^{B \rightarrow A} = \text{softmax} \left(\frac{\mathbf{K}_A \mathbf{q}_i^B}{\sqrt{d}} \right) \quad (7)$$

where $\mathbf{q}_i^K \in \mathbf{Q}_K$, and $\mathbf{Q}_K, \mathbf{K}_K \in \mathbb{R}^{N_K \times d}$ are the query and key values (respectively) for object \mathcal{K} associated with cross-object attention Transformer module $g_{\mathcal{T}_K}$ (see Appendix C for details). These weights are then used to compute the virtual soft correspondences $\mathbf{V}_A, \mathbf{V}_B$ using Equation 5.

Adjustment via Correspondence Residuals: As previously stated, the virtual soft correspondences $\mathbf{V}_A, \mathbf{V}_B$ given by Equations 5a and 5b are constrained to be within the convex hull of each object. However, many relative placement tasks cannot be solved perfectly with this constraint. For instance, we might want a point on the handle of a teapot to correspond to some point above a stovetop (which lies outside the convex hull of the points on the stovetop). To allow for such off-object correspondences, we further learn a *residual vector*, $\delta_i^A \in \Delta_A$ for each point i that corrects each virtual corresponding point \mathbf{v}_i^A . This allows us to displace each virtual corresponding point to any arbitrary location that might be suitable for the task. To compute these residual vectors, we use a point-wise neural network $g_{\mathcal{R}_A}, g_{\mathcal{R}_B}$ to map each point’s embedding into a 3D residual vector:

$$\delta_i^A = g_{\mathcal{R}_A}(\phi_i^A) \in \mathbb{R}^3, \quad \delta_i^B = g_{\mathcal{R}_B}(\phi_i^B) \in \mathbb{R}^3$$

Applying these residual offsets to the virtual points, we get a set of *corrected virtual correspondences*, $\tilde{\mathbf{v}}_i^A \in \tilde{\mathbf{V}}_A$ and $\tilde{\mathbf{v}}_i^B \in \tilde{\mathbf{V}}_B$, defined as

$$\tilde{\mathbf{v}}_i^A = \mathbf{v}_i^A + \delta_i^A, \quad \tilde{\mathbf{v}}_i^B = \mathbf{v}_i^B + \delta_i^B \quad (8)$$

These corrected virtual correspondences $\tilde{\mathbf{v}}_i^A$ define the estimated goal location relative to object \mathcal{B} for each point $\mathbf{p}_i \in \mathbf{P}_A$ of object \mathcal{A} , and likewise for each point in object \mathcal{B} (see visualization in Appendix A.1).

Least-Squares Cross-Pose Optimization with Weighted SVD: Given the sets of dense correspondences, $(\mathbf{P}_A, \tilde{\mathbf{V}}_A)$ and $(\mathbf{P}_B, \tilde{\mathbf{V}}_B)$, we would like to compute a single rigid transformation for object \mathcal{A} . To do so, we solve for the transformation \mathbf{T}_{AB} (the cross-pose) that minimizes the weighted distance between each point and its corrected virtual correspondence. Formally, this leads to the following weighted least squares optimization:

$$\mathcal{J}(\mathbf{T}_{AB}) = \sum_{i=1}^{N_A} \alpha_i^A \|\mathbf{T}_{AB} \mathbf{p}_i^A - \tilde{\mathbf{v}}_i^A\|_2^2 + \sum_{i=1}^{N_B} \alpha_i^B \|\mathbf{T}_{AB}^{-1} \mathbf{p}_i^B - \tilde{\mathbf{v}}_i^B\|_2^2 \quad (9)$$

where the weights $\alpha_i^A \in \alpha_A$, $\alpha_i^B \in \alpha_B$ signify the importance of each correspondence and are predicted by a point-wise MLP as shown in Figure 4. These weights are learned end-to-end as

parameters of our network; they are visualized in Appendix A.2, which shows that the network has learned to assign more weight to the parts of the object that are most important for the task, such as the region around the mug handle (on the mug) and the region around the peg (on the rack). Equation 9 is the well-known weighted Procrustes problem, for which there exists an analytical solution. To maintain the differentiability of the system, we use a weighted differentiable SVD operation [29] to compute the cross-pose \mathbf{T}_{AB} that minimizes this objective (see Appendix D for details). This allows us to train the system end-to-end as described below.

4.2 TAX-Pose Training Pipeline

To train our model, we use a segmented set of demonstration point clouds of a pair of objects in the goal configuration. For each demonstration point cloud, we generate multiple training examples by transforming each object’s point cloud, \mathbf{P}_A and \mathbf{P}_B by random SE(3) transformations \mathbf{T}_α and \mathbf{T}_β , respectively. The predicted cross-pose, \mathbf{T}_{AB} , is then compared with the ground truth cross-pose, $\mathbf{T}_{AB}^{GT} := \mathbf{T}_\beta \mathbf{T}_\alpha^{-1}$, using an average distance loss [30] with dense regularization (see more details on our training losses in Appendix E.1).

5 Experiments

To evaluate TAX-Pose, we conduct a wide range of simulated and real-world experiments on two classes of relative placement tasks: NDF [14] Tasks and PartNet-Mobility Placement Tasks. All tasks involve placing an “action” object at a specific location relative to an anchor object, in which the relative pose is specified by a set of demonstrations. Our method then generalizes to perform this task on novel objects in unseen configurations. We refer the reader to our [project website](#) for additional results and videos.

5.1 NDF Tasks

We evaluate our method on all three NDF [14, 31] tasks (*mug hanging*, *bottle placement*, and *bowl placement*); see Appendix F.1.3 for results on *bottle* and *bowl* placement. Results on *mug hanging* are described in more detail below.

Simulation Experiments: For our simulation experiments, we perform the task of hanging a mug on a rack as two sequential cross-pose estimation steps: grasping the mug (estimating the cross-pose between the gripper and the mug) and hanging the mug on the rack (estimating the cross-pose between the mug and the rack). In Pybullet [32, 33, 34], we simulate a Franka Panda above a table with 4 depth cameras placed on the corners of the table. The model is trained on 10 simulated demonstrations of mug hanging. We evaluate task execution success on unseen mug instances in randomly generated initial configurations. We measure task success rates of 1) *Grasping*, where success is achieved when the object is grasped stably; 2) *Placing*, where success is achieved when the mug is placed stably on the rack; 3) *Overall*, when the predicted transforms enable both grasp and place success in sequence. We compare our method to Neural Descriptor Field (NDF) [14] and Dense Object Nets (DON) [12]. Details of these methods can be found in prior work [14, 15].

Simulation Results: We evaluate our method in simulation in 100 trials consisting of unseen *mug* instances in random initial and goal configurations for both **Upright** and **Arbitrary** poses. As shown in Table 1, our method significantly outperforms the baselines for simulated mug hanging. We report additional results for simulated *bottle* and *bowl* placement tasks in Table 8 in Appendix F.1.3.

Ablation Analysis: Effects of Number of Demonstrations. To study how the number of demonstrations observed affects our method’s performance, we train our model on {10, 5, 1} demonstrations of upright pose mug hanging. Results are found in Table 2. Our method outperforms the baselines for all number of demonstrations; TAX-Pose can perform well even with as few as 5 demonstrations.

Cross-Pose Estimation Design Choices. We analyze the effects of design choices made in our Cross-Pose estimation algorithm for the upright pose mug hanging task. Specifically, we analyze the



Figure 5: Real-world experiments summary. **Left:** In object placement task, we train using simulated demonstrations and test on real-world objects. **Right:** Mug Hanging real-world experiments. We train from just 10 demonstrations from 10 training mugs in the real world and test on 10 unseen test mugs.

effects of 1) computing residual correspondence; 2) the use of *weighted* SVD over non-weighted in computing cross-pose; 3) using a transformer as the cross-object attention, as opposed to simpler model such as a 3-layer MLP. Table 3 shows that each major component of our system is important for task success. See more ablation experiments in Appendix F.1.1.

	Grasp	Place	Overall	Grasp	Place	Overall	Model	# Demos Used			Ablation	Grasp	Place	Overall
	Upright Pose			Arbitrary Pose				1	5	10		No Res.	0.97	0.96
DON [12]	0.91	0.50	0.45	0.35	0.45	0.17	DON [12]	0.32	0.36	0.45	No Res.	0.97	0.96	0.93
NDF [14]	0.96	0.92	0.88	0.78	0.75	0.58	NDF [14]	0.46	0.70	0.88	Unw. SVD	0.92	0.94	0.88
TAX-Pose	0.99	0.97	0.96	0.75	0.84	0.63	TAX-Pose	0.77	0.90	0.96	No Attn.	0.90	0.82	0.76
											TAX-Pose	0.99	0.97	0.96

Table 1: Mug on rack simulation success rate (\uparrow)

Table 2: # Demos vs.

Table 3: Mug hanging abla-

Overall success rate (\uparrow)

tions success rate (\uparrow)

Real-World Experiments: We explore the hanging component of the mug on a rack task in a real world environment, which requires estimating the cross-pose between the mug and the rack. We train TAX-Pose using real demonstrations of 10 different mugs hung on a rack (1 demonstration each, for a total of only 10 real-world demonstrations for training). A motion primitive is used to grasp each mug, after which the robot plans a trajectory to apply the predicted cross-pose to the grasped mug. We evaluate the model on the 10 training mugs in novel poses, as well as on 10 unseen mugs (see Figure 5). For each of the 20 mugs, we conduct 5 trials, varying the mug’s and rack’s starting poses in each trial. Success is recorded if a peg penetrates the mug handle at the end of the trial. Our method achieves a success rate of 62% on training mugs in novel poses and 54% on unseen mugs. A visualization of the results can be seen in Figure 5 (right) and on the [project website](#). Note that our method is able to perform the mug hanging task while varying the pose of the mug rack (see our [project website](#)), whereas the baselines (NDF [14], DON [12]) cannot because they assume a fixed, known rack position (see NDF [14] for baseline details).

5.2 PartNet-Mobility Placement Tasks

Task Description: We also define a PartNet-Mobility Placement task as placing a given action object relative to an anchor object based on a semantic goal position. We select a set of household furniture objects from the PartNet-Mobility dataset [35] as the anchor objects, and a set of small rigid objects released with the Ravens simulation environment [36, 37, 38, 39] as the action objects. For each anchor object, we define a set of semantic goal positions (i.e. ‘top’, ‘left’, ‘right’, ‘in’), where action objects should be placed relative to each anchor. Each semantic goal position defines a unique task in our cross-pose prediction framework. Given a synthetic point cloud observation of both objects, the task is to predict a cross-pose that places the object at the specific semantic goal. We evaluate both a *goal-conditioned* variant (**TAX-Pose GC**), which is trained across all goals, and a *task-specific* variant (**TAX-Pose**) of our model, which trains a separate model per goal type (see Appendix F.2.2 for details). In both cases we train only 1 model across all action and anchor objects. All models are trained entirely on simulated data and transfer directly to real-world with no finetuning. Further task details can be found in the Appendix G.2.

Baselines: We compare our method to a variety of end-to-end imitation-learning-based methods trained from a motion planner expert in simulation (see Appendix G.2.4 for details). Note that in the PartNet-Mobility Placement experiments, the pose of the anchor object poses are randomly varied. As such, we omit a comparison to methods that assume a static anchor, such as the Neural Descriptor

Field (NDF) [14, 40] and Dense Object Nets (DON) [12, 41] baselines used in the mug hanging task (Section 5.1), as both methods assume that the anchor objects are in a fixed, known position.

Results: We report rotation (\mathcal{E}_R) and translation (\mathcal{E}_t) error between our predicted transform and the ground truth as geodesic rotational distance [42, 43, 44, 45] and L_2 distance, respectively. In both our simulated experiments (Table 4 Top) and our real-world experiments (Table 4 Bottom), we find that TAX-Pose outperforms the baseline end-to-end imitation learning methods, with the *goal-conditioned* variant, TAX-Pose GC, performing the best. In real-world experiments, our method generalizes to novel distributions of starting poses better than the Goal Flow baseline, placing action objects into the goal regions with a 92% success rate. See Figure 5 (left) and the [website](#) for results; see Appendix F.2 for more detailed tables and Appendix G.2.4 for baseline details.

	Average	
	\mathcal{E}_R	\mathcal{E}_t
E2E BC	42.26	0.73
E2E DAgger	37.96	0.69
Traj. Flow	35.95	0.67
Goal Flow	26.64	0.17
TAX-Pose	6.64	0.16
TAX-Pose GC	4.94	0.16

	Average SR
	Goal Flow
TAX-Pose	0.92

Table 4: **Top:** Simulation Rotational ($^\circ$) and Translational (m) Errors (\downarrow). **Bottom:** Real-world goal placement success rate (\uparrow).

6 Conclusion and Limitations

In this paper, we show that dense soft correspondence can be used to learn task specific object relationships that generalize to novel object instances. Correspondence residuals allow our method to estimate correspondences to virtual points, outside of the objects convex hull, drastically increasing the number of tasks this method can complete. We further show that this “cross-pose” can be learned for a task, using a small number of demonstrations. Finally, we show that our method far outperforms the baselines on two challenging tasks in both real and simulated experiments. While our method is able to predict relative pose relationships with high precision, it has several limitations:

- **Requires segmentation:** Our method requires an accurate segmentation of two objects in order to predict their relative goal pose.
- **Performance degrades under occlusion:** Our method performs best when complete point clouds are provided, captured via multiple cameras or by repeatedly reorienting the objects.
- **Poorly defined for multimodal relationships:** Because our method extracts a single global estimate of relative pose from a fixed set of correspondences, performance on objects with multiple valid goals is not well-defined. Our method might be augmented with a consensus-based or sampling-based approach to capture the multimodality of the solution space in these cases. We leave this for future work.

Acknowledgements

This material is based upon work supported by the National Science Foundation under Grant No. IIS-1849154. This work was also supported by LG Electronics. We are grateful to Daniel Seita and Jenny Wang for their helpful feedback and discussion on the paper.

References

- [1] D. G. Lowe. Object recognition from local scale-invariant features. In *Proceedings of the seventh IEEE international conference on computer vision*, volume 2, pages 1150–1157. Ieee, 1999.
- [2] F. Rothganger, S. Lazebnik, C. Schmid, and J. Ponce. 3d object modeling and recognition using local affine-invariant image descriptors and multi-view spatial constraints. *International journal of computer vision*, 66(3):231–259, 2006.
- [3] Y. Xiang, T. Schmidt, V. Narayanan, and D. Fox. Posecnn: A convolutional neural network for 6d object pose estimation in cluttered scenes. *Robotics: Science and Systems (RSS)*, 2018.

- [4] Y. He, W. Sun, H. Huang, J. Liu, H. Fan, and J. Sun. Pvn3d: A deep point-wise 3d keypoints voting network for 6dof pose estimation. In *Proceedings of the IEEE/CVF conference on computer vision and pattern recognition*, pages 11632–11641, 2020.
- [5] Y. He, H. Huang, H. Fan, Q. Chen, and J. Sun. Ffb6d: A full flow bidirectional fusion network for 6d pose estimation. In *Proceedings of the IEEE/CVF Conference on Computer Vision and Pattern Recognition*, pages 3003–3013, 2021.
- [6] D. Turpin, L. Wang, S. Tsogkas, S. Dickinson, and A. Garg. Gift: Generalizable interaction-aware functional tool affordances without labels. *Robotics: Science and Systems (RSS)*, 2021.
- [7] L. Manuelli, W. Gao, P. Florence, and R. Tedrake. kpm: Keypoint affordances for category-level robotic manipulation. *International Symposium on Robotics Research (ISRR) 2019*, 2019.
- [8] Z. Qin, K. Fang, Y. Zhu, L. Fei-Fei, and S. Savarese. Keto: Learning keypoint representations for tool manipulation. In *2020 IEEE International Conference on Robotics and Automation (ICRA)*, pages 7278–7285. IEEE, 2020.
- [9] M. Vecerik, J.-B. Regli, O. Sushkov, D. Barker, R. Pevcevičute, T. Rothörl, R. Hadsell, L. Agapito, and J. Scholz. S3k: Self-supervised semantic keypoints for robotic manipulation via multi-view consistency. In *Conference on Robot Learning*, pages 449–460. PMLR, 2021.
- [10] L. Manuelli, Y. Li, P. Florence, and R. Tedrake. Keypoints into the future: Self-supervised correspondence in model-based reinforcement learning. In *Conference on Robot Learning*, pages 693–710. PMLR, 2021.
- [11] C. Pan, B. Okorn, H. Zhang, B. Eisner, and D. Held. Tax-pose: Task-specific cross-pose estimation for robot manipulation. In *Conference on Robot Learning*, pages 1783–1792. PMLR, 2023.
- [12] P. R. Florence, L. Manuelli, and R. Tedrake. Dense object nets: Learning dense visual object descriptors by and for robotic manipulation. In *Conference on Robot Learning*, pages 373–385. PMLR, 2018.
- [13] H. Zhang. Health diagnosis based on analysis of data captured by wearable technology devices. *International Journal of Advanced Science and Technology*, 95:89–96, 2016.
- [14] A. Simeonov, Y. Du, A. Tagliasacchi, J. B. Tenenbaum, A. Rodriguez, P. Agrawal, and V. Sitzmann. Neural descriptor fields: Se (3)-equivariant object representations for manipulation. In *2022 International Conference on Robotics and Automation (ICRA)*, pages 6394–6400. IEEE, 2022.
- [15] H. Zhang, J. Ichnowski, D. Seita, J. Wang, H. Huang, and K. Goldberg. Robots of the lost arc: Self-supervised learning to dynamically manipulate fixed-endpoint cables. In *2021 IEEE International Conference on Robotics and Automation (ICRA)*, pages 4560–4567. IEEE, 2021.
- [16] H. Zhang, B. Eisner, and D. Held. Flowbot++: Learning generalized articulated objects manipulation via articulation projection. *arXiv preprint arXiv:2306.12893*, 2023.
- [17] K. C. Sim, F. Beaufays, A. Benard, D. Guliani, A. Kabel, N. Khare, T. Lucassen, P. Zadrazil, H. Zhang, L. Johnson, et al. Personalization of end-to-end speech recognition on mobile devices for named entities. In *2019 IEEE Automatic Speech Recognition and Understanding Workshop (ASRU)*, pages 23–30. IEEE, 2019.
- [18] P. J. Besl and N. D. McKay. Method for registration of 3-d shapes. In *Sensor fusion IV: control paradigms and data structures*, volume 1611, pages 586–606. Spie, 1992.

- [19] H. Zhang, J. Ichnowski, Y. Avigal, J. Gonzales, I. Stoica, and K. Goldberg. Dex-net ar: Distributed deep grasp planning using a commodity cellphone and augmented reality app. In *2020 IEEE International Conference on Robotics and Automation (ICRA)*, pages 552–558. IEEE, 2020.
- [20] S. Bouaziz, A. Tagliasacchi, and M. Pauly. Sparse iterative closest point. In *Computer graphics forum*, volume 32, pages 113–123. Wiley Online Library, 2013.
- [21] S. Rusinkiewicz and M. Levoy. Efficient variants of the icp algorithm. In *Proceedings third international conference on 3-D digital imaging and modeling*, pages 145–152. IEEE, 2001.
- [22] A. Segal, D. Haehnel, and S. Thrun. Generalized-icp. In *Robotics: science and systems*, volume 2, page 435. Seattle, WA, 2009.
- [23] G. Agamennoni, S. Fontana, R. Y. Siegwart, and D. G. Sorrenti. Point clouds registration with probabilistic data association. In *2016 IEEE/RSJ International Conference on Intelligent Robots and Systems (IROS)*, pages 4092–4098. IEEE, 2016.
- [24] T. Hinzmann, T. Stastny, G. Conte, P. Doherty, P. Rudol, M. Wzorek, E. Galceran, R. Siegwart, and I. Gilitschenski. Collaborative 3d reconstruction using heterogeneous uavs: System and experiments. In *International Symposium on Experimental Robotics*, pages 43–56. Springer, 2016.
- [25] D. Hähnel and W. Burgard. Probabilistic matching for 3d scan registration. In *Proc. of the VDI-Conference Robotik*, volume 2002. Citeseer, 2002.
- [26] Y. Wang and J. M. Solomon. Deep closest point: Learning representations for point cloud registration. In *Proceedings of the IEEE/CVF International Conference on Computer Vision*, pages 3523–3532, 2019.
- [27] A. V. Phan, M. Le Nguyen, Y. L. H. Nguyen, and L. T. Bui. Dgcnn: A convolutional neural network over large-scale labeled graphs. *Neural Networks*, 108:533–543, 2018.
- [28] A. Vaswani, N. Shazeer, N. Parmar, J. Uszkoreit, L. Jones, A. N. Gomez, Ł. Kaiser, and I. Polosukhin. Attention is all you need. *Advances in neural information processing systems*, 30, 2017.
- [29] T. Papadopoulos and M. I. Lourakis. Estimating the jacobian of the singular value decomposition: Theory and applications. In *European Conference on Computer Vision*, pages 554–570. Springer, 2000.
- [30] S. Hinterstoisser, V. Lepetit, S. Ilic, S. Holzer, G. Bradschi, K. Konolige, and N. Navab. Model based training, detection and pose estimation of texture-less 3d objects in heavily cluttered scenes. In *Asian conference on computer vision*, pages 548–562. Springer, 2012.
- [31] S. Devgon, J. Ichnowski, A. Balakrishna, H. Zhang, and K. Goldberg. Orienting novel 3d objects using self-supervised learning of rotation transforms. In *2020 IEEE 16th International Conference on Automation Science and Engineering (CASE)*, pages 1453–1460. IEEE, 2020.
- [32] E. Coumans and Y. Bai. Pybullet, a python module for physics simulation for games, robotics and machine learning, 2016–2020.
- [33] Y. Avigal, S. Paradis, and H. Zhang. 6-dof grasp planning using fast 3d reconstruction and grasp quality cnn. *arXiv preprint arXiv:2009.08618*, 2020.
- [34] Y. Avigal, V. Satish, Z. Tam, H. Huang, H. Zhang, M. Danielczuk, J. Ichnowski, and K. Goldberg. Avplug: Approach vector planning for unicontract grasping amid clutter. In *2021 IEEE 17th International Conference on Automation Science and Engineering (CASE)*, pages 1140–1147. IEEE, 2021.

- [35] F. Xiang, Y. Qin, K. Mo, Y. Xia, H. Zhu, F. Liu, M. Liu, H. Jiang, Y. Yuan, H. Wang, and Others. Sapien: A simulated part-based interactive environment. In *Proceedings of the IEEE/CVF Conference on Computer Vision and Pattern Recognition*, pages 11097–11107, 2020.
- [36] A. Zeng, P. Florence, J. Tompson, S. Welker, J. Chien, M. Attarian, T. Armstrong, I. Krasin, D. Duong, V. Sindhwani, et al. Transporter networks: Rearranging the visual world for robotic manipulation. In *Conference on Robot Learning*, pages 726–747. PMLR, 2021.
- [37] Y. Yao, S. Deng, Z. Cao, H. Zhang, and L.-J. Deng. Apla: Additional perturbation for latent noise with adversarial training enables consistency. *arXiv preprint arXiv:2308.12605*, 2023.
- [38] D. Jin, S. Karmalkar, H. Zhang, and L. Carlone. Multi-model 3d registration: Finding multiple moving objects in cluttered point clouds. *arXiv preprint arXiv:2402.10865*, 2024.
- [39] S. Shen, Z. Zhu, L. Fan, H. Zhang, and X. Wu. Diffclip: Leveraging stable diffusion for language grounded 3d classification. In *Proceedings of the IEEE/CVF Winter Conference on Applications of Computer Vision*, pages 3596–3605, 2024.
- [40] V. Lim, H. Huang, L. Y. Chen, J. Wang, J. Ichnowski, D. Seita, M. Laskey, and K. Goldberg. Planar robot casting with real2sim2real self-supervised learning. *arXiv preprint arXiv:2111.04814*, 2021.
- [41] V. Lim, H. Huang, L. Y. Chen, J. Wang, J. Ichnowski, D. Seita, M. Laskey, and K. Goldberg. Real2sim2real: Self-supervised learning of physical single-step dynamic actions for planar robot casting. In *2022 International Conference on Robotics and Automation (ICRA)*, pages 8282–8289. IEEE, 2022.
- [42] D. Q. Huynh. Metrics for 3d rotations: Comparison and analysis. *Journal of Mathematical Imaging and Vision*, 35(2):155–164, 2009.
- [43] R. Hartley, J. Trumpf, Y. Dai, and H. Li. Rotation averaging. *International journal of computer vision*, 103(3):267–305, 2013.
- [44] A. Elmquist, A. Young, T. Hansen, S. Ashokkumar, S. Caldararu, A. Dashora, I. Mahajan, H. Zhang, L. Fang, H. Shen, et al. Art/atk: A research platform for assessing and mitigating the sim-to-real gap in robotics and autonomous vehicle engineering. *arXiv preprint arXiv:2211.04886*, 2022.
- [45] S. Teng, H. Zhang, D. Jin, A. Jasour, M. Ghaffari, and L. Carlone. Gmkf: Generalized moment kalman filter for polynomial systems with arbitrary noise. *arXiv preprint arXiv:2403.04712*, 2024.
- [46] Y. Li, G. Wang, X. Ji, Y. Xiang, and D. Fox. Deepim: Deep iterative matching for 6d pose estimation. In *Proceedings of the European Conference on Computer Vision (ECCV)*, pages 683–698, 2018.
- [47] Y. Wang, Y. Sun, Z. Liu, S. E. Sarma, M. M. Bronstein, and J. M. Solomon. Dynamic graph cnn for learning on point clouds. *Acm Transactions On Graphics (tog)*, 38(5):1–12, 2019.
- [48] A. v. d. Oord, Y. Li, and O. Vinyals. Representation learning with contrastive predictive coding. *arXiv preprint arXiv:1807.03748*, 2018.
- [49] A. X. Chang, T. Funkhouser, L. Guibas, P. Hanrahan, Q. Huang, Z. Li, S. Savarese, M. Savva, S. Song, H. Su, J. Xiao, L. Yi, and F. Yu. ShapeNet: An Information-Rich 3D Model Repository. Technical Report arXiv:1512.03012 [cs.GR], Stanford University — Princeton University — Toyota Technological Institute at Chicago, 2015.
- [50] K. He, X. Zhang, S. Ren, and J. Sun. Delving deep into rectifiers: Surpassing human-level performance on imagenet classification. In *Proceedings of the IEEE international conference on computer vision*, pages 1026–1034, 2015.

- [51] C. Deng, O. Litany, Y. Duan, A. Poulencard, A. Tagliasacchi, and L. J. Guibas. Vector neurons: A general framework for so (3)-equivariant networks. In *Proceedings of the IEEE/CVF International Conference on Computer Vision*, pages 12200–12209, 2021.
- [52] S. Ross, G. Gordon, and D. Bagnell. A reduction of imitation learning and structured prediction to no-regret online learning. In *Proceedings of the fourteenth international conference on artificial intelligence and statistics*, pages 627–635. JMLR Workshop and Conference Proceedings, 2011.
- [53] B. Eisner*, H. Zhang*, and D. Held. Flowbot3d: Learning 3d articulation flow to manipulate articulated objects. In *Robotics: Science and Systems (RSS)*, 2022.
- [54] V. Zeng, T. E. Lee, J. Liang, and O. Kroemer. Visual identification of articulated object parts. In *2021 IEEE/RSJ International Conference on Intelligent Robots and Systems (IROS)*, pages 2443–2450. IEEE, 2020.
- [55] M. Danielczuk, A. Mousavian, C. Eppner, and D. Fox. Object rearrangement using learned implicit collision functions. In *2021 IEEE International Conference on Robotics and Automation (ICRA)*, pages 6010–6017. IEEE, 2021.
- [56] W. E. Lorensen and H. E. Cline. Marching cubes: A high resolution 3d surface construction algorithm. *ACM siggraph computer graphics*, 21(4):163–169, 1987.
- [57] J. Pan, S. Chitta, and D. Manocha. Fcl: A general purpose library for collision and proximity queries. In *2012 IEEE International Conference on Robotics and Automation*, pages 3859–3866. IEEE, 2012.
- [58] I. A. Sucas, M. Moll, and L. E. Kavraki. The open motion planning library. *IEEE Robotics & Automation Magazine*, 19(4):72–82, 2012.
- [59] A. Hornung, K. M. Wurm, M. Bennewitz, C. Stachniss, and W. Burgard. Octomap: An efficient probabilistic 3d mapping framework based on octrees. *Autonomous robots*, 34(3):189–206, 2013.
- [60] C. R. Qi, L. Yi, H. Su, and L. J. Guibas. Pointnet++: Deep hierarchical feature learning on point sets in a metric space. *Advances in neural information processing systems*, 30, 2017.

Appendix

A	Visual Explanations of TAX-Pose	15
A.1	Illustration of Corrected Virtual Correspondence	15
A.2	Learned Importance Weights	15
B	Proof of TAX-Pose Translational Equivariance	16
C	Description of Cross-Object Attention Weight Computation	17
C.1	Ablation	18
D	Description of Weighted SVD	19
E	Training Details	19
E.1	Supervision	19
E.2	Pretraining	20
E.3	Architectural Variants	20
F	Additional Results	21
F.1	NDF Placement Tasks	21
F.1.1	Further Ablations on Mug Hanging Task	21
F.1.2	Effects of Pretraining on Mug Hanging Task	22
F.1.3	Additional Simulation Experiments on Bowl and Bottle Placement Task	23
F.1.4	Failure Cases	24
F.2	PartNet-Mobility Tasks	25
F.2.1	Expanded Results Tables	25
F.2.2	Goal-Conditioned Variant	27
F.2.3	Failure Cases	27
G	Task Details	27
G.1	NDF Task Details	27
G.1.1	Baseline Description	28
G.1.2	Training Data	28
G.1.3	Training and Inference	28
G.1.4	Motion Planning	28
G.1.5	Real-World Experiments	28
G.2	PartNet-Mobility Object Placement Task Details	29
G.2.1	Dataset Preparation	29
G.2.2	Metrics	29
G.2.3	Motion Planning	30

H Author Contributions **31**

A Visual Explanations of TAX-Pose

A.1 Illustration of Corrected Virtual Correspondence

The virtual corresponding points, $\mathbf{V}_A, \mathbf{V}_B$ given by Equation 3 in the main text, are constrained to be within the convex hull of each object. However, correspondences which are constrained to the convex hull are insufficient to express a large class of desired tasks. For instance, we might want a point on the handle of a teapot to correspond to some point above a stovetop, which lies outside the convex hull of the points on the stovetop. To allow for such placements, for each point-wise embedding ϕ_i , we further learn a *residual vector*, $\delta_i^A \in \Delta_A$ that corrects each virtual corresponding point, allowing us to displace each virtual corresponding point to any arbitrary location that might be suitable for the task. Concretely, we use a point-wise neural network $g_{\mathcal{R}}$ which maps each embedding into a 3D residual vector:

$$\delta_i^A = g_{\mathcal{R}}(\phi_i^A) \in \mathbb{R}^3, \delta_i^B = g_{\mathcal{R}}(\phi_i^B) \in \mathbb{R}^3$$

Applying these to the virtual points, we get a set of *corrected virtual correspondences*, $\tilde{\mathbf{v}}_i^A \in \tilde{\mathbf{V}}_A$ and $\tilde{\mathbf{v}}_i^B \in \tilde{\mathbf{V}}_B$, defined as

$$\tilde{\mathbf{v}}_i^A = \mathbf{v}_i^A + \delta_i^A, \tilde{\mathbf{v}}_i^B = \mathbf{v}_i^B + \delta_i^B \tag{10}$$

These corrected virtual correspondences $\tilde{\mathbf{v}}_i^A$ define the estimated goal location relative to object \mathcal{B} for each point $\mathbf{p}_i \in \mathbf{P}_A$ in object \mathcal{A} , and likewise for each point in object \mathcal{B} , as shown in Figure 6.

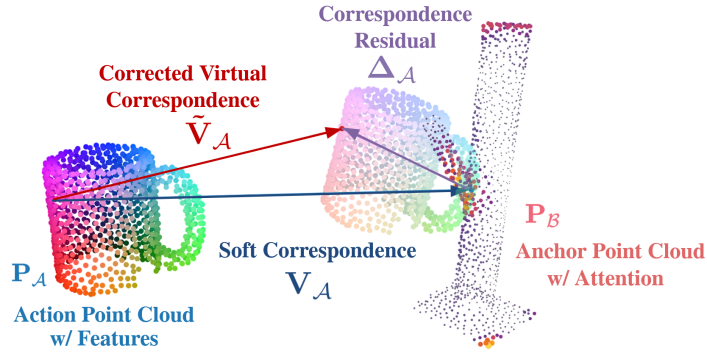


Figure 6: Computation of Corrected Virtual Correspondence. Given a pair of object point clouds $\mathbf{P}_A, \mathbf{P}_B$, a per-point *soft correspondence* \mathbf{V}_A is first computed. Next, to allow the predicted correspondence to lie beyond object’s convex hull, these soft correspondences are adjusted with *correspondence residuals*, Δ_A , which results in the *corrected virtual correspondence*, $\tilde{\mathbf{V}}_A$. The coloring scheme and the point size on the rack represent the the value of the the attention weights, where the more red and larger the point, the higher the attention weights, the more gray and smaller the point the lower the attention weights.

A.2 Learned Importance Weights

A visualization of the learned importance weights, α_A and α_B for the mug and rack are visualized by both color scheme and point size in Figure 7

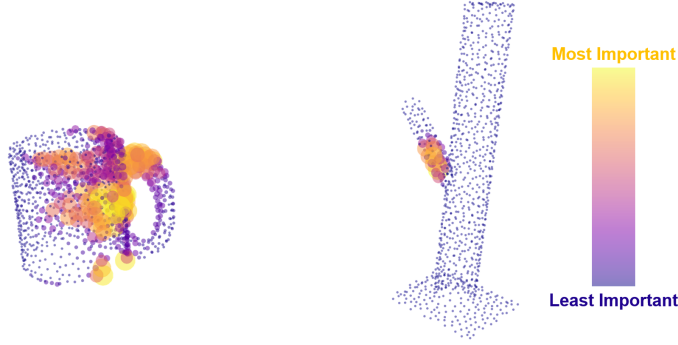


Figure 7: Learned Importance Weights for Weighted SVD on Mug and Rack. The coloring scheme and the point size on both objects represent the value of the learned importance weights, where the more yellow and larger the point, the higher the learned importance weights, the more purple and smaller the point the lower the learned importance weights.

B Proof of TAX-Pose Translational Equivariance

One benefit of our method is that it is translationally equivariant by construction. This means that if the object point clouds, \mathbf{P}_A and \mathbf{P}_B , are translated by random translation \mathbf{t}_α and \mathbf{t}_β , respectively, i.e. $\mathbf{P}_{A'} = \mathbf{P}_A + \mathbf{t}_\alpha$ and $\mathbf{P}_{B'} = \mathbf{P}_B + \mathbf{t}_\beta$, then the resulting corrected virtual correspondences, $\tilde{\mathbf{V}}_B$ and $\tilde{\mathbf{V}}_A$, respectively, are transformed accordingly, i.e. $\tilde{\mathbf{V}}_B + \mathbf{t}_\beta$ and $\tilde{\mathbf{V}}_A + \mathbf{t}_\alpha$, respectively, as we will show below. This results in an estimated cross-pose transformation that is also equivariant to translation by construction. This is achieved because our learned features and correspondence residuals are invariant to translation, and our virtual correspondence points are equivariant to translation.

First, our point features are a function of centered point clouds. That is, given point clouds \mathbf{P}_A and \mathbf{P}_B , the mean of each point cloud is computed as

$$\bar{\mathbf{p}}_k = \frac{1}{N_k} \sum_{i=1}^{N_k} \mathbf{P}_k.$$

This mean is then subtracted from the clouds,

$$\bar{\mathbf{P}}_k = \mathbf{P}_k - \bar{\mathbf{p}}_k,$$

which centers the cloud at the origin. The features are then computed on the centered point clouds:

$$\Phi_k = g_k(\bar{\mathbf{P}}_k).$$

Since the point clouds are centered before features are computed, the features Φ_k are invariant to an arbitrary translation $\mathbf{P}_{k'} = \mathbf{P}_k + \mathbf{t}_{\kappa}$.

These translationally invariant features are then used, along with the original point clouds, to compute “corrected virtual points” as a combination of virtual correspondence points, $\mathbf{v}_i^{k'}$ and the correspondence residuals, $\delta_i^{k'}$. As we will see below, the “corrected virtual points” will be translationally equivariant by construction.

The virtual correspondence points, $\mathbf{v}_i^{k'}$, are computed using weights that are a function of only the translationally invariant query and key values from the cross-object attention transformer $g_{\mathcal{T}_K}$, \mathbf{Q}_K and \mathbf{K}_K , which are in turn functions of only the translationally invariant features, Φ_k :

$$\mathbf{w}_i^{A' \rightarrow B'} = \text{softmax} \left(\frac{\mathbf{K}_{B'} \mathbf{q}_i^{A'}}{\sqrt{d}} \right) = \text{softmax} \left(\frac{\mathbf{K}_B \mathbf{q}_i^A}{\sqrt{d}} \right) = \mathbf{w}_i^{A \rightarrow B}$$

thus the weights are also translationally invariant. These translationally invariant weights are applied to the translated cloud

$$\mathbf{v}_i^{A'} = \mathbf{P}_B \mathbf{w}_i^{A \rightarrow B} = (\mathbf{P}_B + \mathbf{t}_\beta) \mathbf{w}_i^{A \rightarrow B} = \sum_j \mathbf{p}_j^B \cdot w_{i,j}^{A \rightarrow B} + \mathbf{t}_\beta \sum_j w_{i,j}^{A \rightarrow B} = \mathbf{P}_B \mathbf{w}_i^{A \rightarrow B} + \mathbf{t}_\beta,$$

since $\sum_{j=1}^{N_B} w_{ij}^{A \rightarrow B} = 1$. Thus the virtual correspondence points $\mathbf{v}_i^{A'}$ are equivalently translated. The same logic follows for the virtual correspondence points $\mathbf{v}_i^{B'}$. This gives us a set of translationally equivariant virtual correspondence points $\mathbf{v}_i^{A'}$ and $\mathbf{v}_i^{B'}$.

The correspondence residuals, $\delta_i^{k'}$, are a direct function of only the translationally invariant features Φ_k ,

$$\delta_i^{k'} = g_{\mathcal{R}_K}(\phi_i^{k'}) = g_{\mathcal{R}_K}(\phi_i^k) = \delta_i^k,$$

therefore they are also translationally invariant.

Since the virtual correspondence points are translationally equivariant, $\mathbf{v}_i^{A'} = \mathbf{v}_i^A + \mathbf{t}_\beta$ and the correspondence residuals are translationally invariant, $\delta_i^{k'} = \delta_i^k$, the final corrected virtual correspondence points, $\tilde{\mathbf{v}}_i^{A'}$, are translationally equivariant, i.e. $\tilde{\mathbf{v}}_i^{A'} = \mathbf{v}_i^A + \delta_i^k + \mathbf{t}_\beta$. This also holds for $\tilde{\mathbf{v}}_i^{B'}$, giving us the final translationally equivariant correspondences between the translated object clouds as $(\mathbf{P}_A + \mathbf{t}_\alpha, \tilde{\mathbf{V}}_B + \mathbf{t}_\beta)$ and $(\mathbf{P}_B + \mathbf{t}_\beta, \tilde{\mathbf{V}}_A + \mathbf{t}_\alpha)$, where $\tilde{\mathbf{V}}_B = [\tilde{\mathbf{v}}_1^A \dots \tilde{\mathbf{v}}_{N_A}^A]^\top$.

As a result, the final computed transformation will be automatically adjusted accordingly. Given that we use weighted SVD to compute the optimal transform, \mathbf{T}_{AB} , with rotational component \mathbf{R}_{AB} and translational component \mathbf{t}_{AB} , the optimal rotation remains unchanged if the point cloud is translated, $\mathbf{R}_{A'B'} = \mathbf{R}_{AB}$, since the rotation is computed as a function of the centered point clouds. The optimal translation is defined as

$$\mathbf{t}_{AB} := \bar{\tilde{\mathbf{v}}}_A - \mathbf{R}_{AB} \cdot \bar{\mathbf{p}}_A,$$

where $\bar{\tilde{\mathbf{v}}}_A$ and $\bar{\mathbf{p}}_A$ are the means of the corrected virtual correspondence points, $\tilde{\mathbf{V}}_B$, and the object cloud \mathbf{P}_A , respectively, for object A . Therefore, the optimal translation between the translated point cloud $\mathbf{P}_{A'}$ and corrected virtual correspondence points $\tilde{\mathbf{V}}^{A'}$ is

$$\begin{aligned} \mathbf{t}_{A'B'} &= \bar{\tilde{\mathbf{v}}}_{A'} - \mathbf{R}_{AB} \cdot \bar{\mathbf{p}}_{A'} \\ &= \bar{\tilde{\mathbf{v}}}_A + \mathbf{t}_\beta - \mathbf{R}_{AB} \cdot (\bar{\mathbf{p}}_A + \mathbf{t}_\alpha) \\ &= \bar{\tilde{\mathbf{v}}}_A + \mathbf{t}_\beta - \mathbf{R}_{AB} \cdot \bar{\mathbf{p}}_A - \mathbf{R}_{AB} \cdot \mathbf{t}_\alpha \\ &= \mathbf{t}_{AB} + \mathbf{t}_\beta - \mathbf{R}_{AB} \cdot \mathbf{t}_\alpha \end{aligned}$$

To simplify the analysis, if we assume that, for a given example, $\mathbf{R}_{AB} = \mathbf{I}$, then we get $\mathbf{t}_{A'B'} = \mathbf{t}_{AB} + \mathbf{t}_\beta - \mathbf{t}_\alpha$, demonstrating that the computed transformation is translation-equivariant by construction.

C Description of Cross-Object Attention Weight Computation

To map our estimated features Ψ_A and Ψ_B obtained from object-specific embedding networks (DGCNN), g_A and g_B respectively, to a set of normalized weight vectors $\mathbf{W}_{A \rightarrow B}$ and $\mathbf{W}_{B \rightarrow A}$, we use the cross attention mechanism of our cross-object attention Transformer module [28]. Following Equations 5a and 5b from the paper, we can extract the desired normalized weight vector $\mathbf{w}_i^{A \rightarrow B}$ for the virtual corresponding point \mathbf{v}_i^A assigned to any point $\mathbf{p}_i^A \in \mathbf{P}^A$ using the intermediate attention embeddings of cross-object attention module as:

$$\mathbf{w}_i^{A \rightarrow B} = \text{softmax} \left(\frac{\mathbf{K}_B \mathbf{q}_i^A}{\sqrt{d}} \right), \quad \mathbf{w}_i^{B \rightarrow A} = \text{softmax} \left(\frac{\mathbf{K}_A \mathbf{q}_i^B}{\sqrt{d}} \right) \quad (11)$$

where $\mathbf{q}_i^K \in \mathbf{Q}_K$, and $\mathbf{Q}_K, \mathbf{K}_K \in \mathbb{R}^{N_K \times d}$ are the query and key (respectively) for object K associated with cross-object attention Transformer module $g_{\mathcal{T}_K}$, as shown in Figure 8. These weights are then used to compute the virtual corresponding points $\mathbf{V}_A, \mathbf{V}_B$ using Equations 5a and 5b in the main paper.

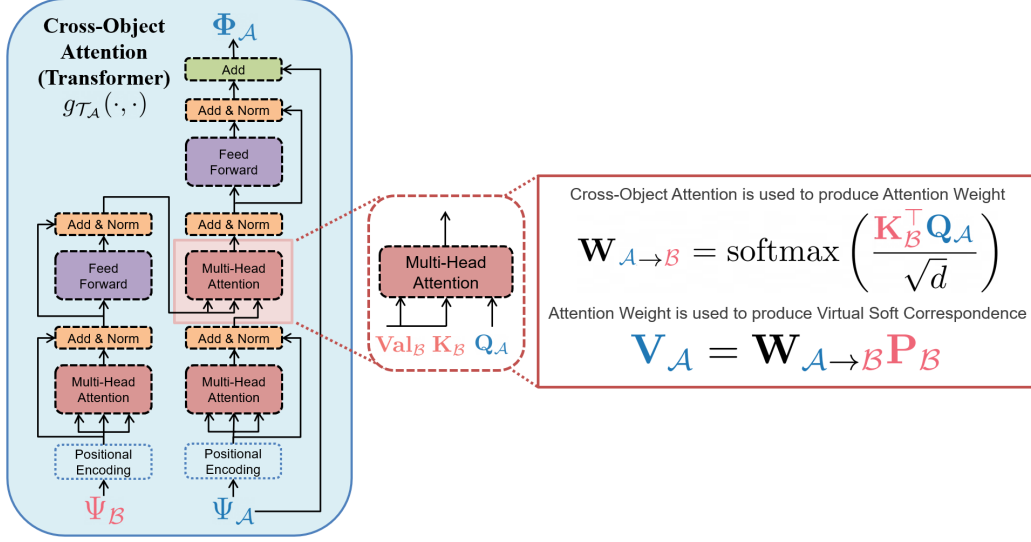


Figure 8: Cross-Object attention weight computation for virtual soft correspondence \mathbf{V}_A from object \mathcal{A} to \mathcal{B} . $\mathbf{Q}_K, \mathbf{K}_K, \mathbf{Val}_K \in \mathbb{R}^{N_K \times d}$ are the query, key and value (respectively) for object \mathcal{K} associated with cross-object attention Transformer module g_{T_K} . The Transformer block is modified from Figure 2(b) in DCP [26].

C.1 Ablation

To explore the importance of this weight computation design choice described in Equation 11, we conducted an ablation experiment on this design choice against an alternative, arguably simpler method for cross-object attention weight computation that was used in prior work [26]. Since the point embeddings ϕ_i^A and ϕ_i^B have the same dimension d , we can select the inner product of the space as a similarity metric between two embeddings.

To compute the virtual corresponding point \mathbf{v}_i^A assigned to any point $\mathbf{p}_i^A \in \mathbf{P}^A$, we can extract the desired normalized weight vector $\mathbf{w}_i^{A \rightarrow B}$ with the softmax function:

$$\mathbf{w}_i^{A \rightarrow B} = \text{softmax}(\Phi_B^\top \phi_i^A), \quad \mathbf{w}_i^{B \rightarrow A} = \text{softmax}(\Phi_A^\top \phi_i^B) \quad (12)$$

This is the approach used in the prior work of Deep Closest Point (DCP) [26]. In the experiments below, we refer to this approach as *point embedding dot-product*.

We conducted an ablation experiment on the weight computation method used in TAX-Pose (Equation 11) against the simpler approach from DCP [26] (Equation 12), on the upright mug hanging task in simulation. The models are trained from 10 demonstrations and tested on 100 trials over the test mug set. As seen in Table 5, the TAX-Pose approach (Equation 11) outperforms *point embedding dot-product* (Equation 12) in all three evaluation categories on *grasp*, *place*, and *overall* in terms of test success rate.

Attention Weight Ablation	Grasp	Place	Overall
Point Embedding Dot-Product (Eqn. 12)	0.83	0.92	0.92
TAX-Pose (Ours) (Eqn. 11)	0.99	0.97	0.96

Table 5: Test success rate (\uparrow) over 100 trials for mug hanging upright task, ablated on attention weight computation methods.

D Description of Weighted SVD

The objective function for computing the optimal rotation and translation given a set of correspondences for object \mathcal{K} , $\{\mathbf{p}_i^k \rightarrow \tilde{\mathbf{v}}_i^k\}_i^{N_k}$ and weights $\{\alpha_i^k\}_i^{N_k}$, is as follows:

$$\mathcal{J}(\mathbf{T}_{AB}) = \sum_{i=1}^{N_A} \alpha_i^A \|\mathbf{T}_{AB} \mathbf{p}_i^A - \tilde{\mathbf{v}}_i^A\|_2^2 + \sum_{i=1}^{N_B} \alpha_i^B \|\mathbf{T}_{AB}^{-1} \mathbf{p}_i^B - \tilde{\mathbf{v}}_i^B\|_2^2$$

First we center (denoted with $*$) the point clouds and virtual points independently, with respect to the learned weights, and stack them into frame-specific matrices (along with weights) retaining their relative position and correspondence:

$$\mathbf{A} = [\mathbf{P}_A^{*\top} \quad \tilde{\mathbf{V}}_B^{*\top}], \quad \mathbf{B} = [\tilde{\mathbf{V}}_A^{*\top} \quad \mathbf{P}_B^{*\top}]^\top, \quad \mathbf{\Gamma} = \text{diag}([\alpha_A \quad \alpha_B])$$

Then the minimizing rotation \mathbf{R}_{AB} is given by:

$$\mathbf{U}\mathbf{\Sigma}\mathbf{V}^\top = \text{svd}(\mathbf{A}\mathbf{\Gamma}\mathbf{B}^\top) \quad (13a) \quad \mathbf{R}_{AB} = \mathbf{U}\mathbf{\Sigma}_* \mathbf{V}^\top \quad (13b)$$

where $\mathbf{\Sigma}_* = \text{diag}([1, 1, \dots, \det(\mathbf{U}\mathbf{V}^\top)])$ and svd is a differentiable SVD operation [29].

The optimal translation can be computed as:

$$\mathbf{t}_A = \bar{\tilde{\mathbf{v}}}_B - \mathbf{R}_{AB} \bar{\mathbf{p}}_A \quad \mathbf{t}_B = \bar{\mathbf{p}}_B - \mathbf{R}_{AB} \bar{\tilde{\mathbf{v}}}_A \quad \mathbf{t} = \frac{N_A}{N} \mathbf{t}_A + \frac{N_B}{N} \mathbf{t}_B \quad (14a)$$

with $N = N_A + N_B$. In the special translation-only case, the optimal translation can be computed by setting \mathbf{R}_{AB} to identity in above equations. The final transform can be assembled:

$$\mathbf{T}_{AB} = \begin{bmatrix} \mathbf{R}_{AB} & \mathbf{t} \\ 0 & 1 \end{bmatrix} \quad (15)$$

E Training Details

E.1 Supervision

To train the encoders $g_A(\bar{\mathbf{P}}_A)$, $g_B(\bar{\mathbf{P}}_B)$ as well as the residual networks $g_{\mathcal{R}_A}(\phi_i^A)$, $g_{\mathcal{R}_B}(\phi_i^B)$, we use a set of losses defined below. We assume we have access to a set of demonstrations of the task, in which the action and anchor objects are in the target relative pose such that $\mathbf{T}_{AB} = \mathbf{I}$.

Point Displacement Loss [3, 46]: Instead of directly supervising the rotation and translation (as is done in DCP), we supervise the predicted transformation using its effect on the points. For this loss, we take the point clouds of the objects in the demonstration configuration, and transform each cloud by a random transform, $\hat{\mathbf{P}}_A = \mathbf{T}_\alpha \mathbf{P}_A$, and $\hat{\mathbf{P}}_B = \mathbf{T}_\beta \mathbf{P}_B$. This would give us a ground truth transform of $\mathbf{T}_{AB}^{GT} = \mathbf{T}_\beta \mathbf{T}_\alpha^{-1}$; the inverse of this transform would move object \mathcal{B} to the correct position relative to object \mathcal{A} . Using this ground truth transform, we compute the MSE loss between the correctly transformed points and the points transformed using our prediction.

$$\mathcal{L}_{\text{disp}} = \|\mathbf{T}_{AB} \mathbf{P}_A - \mathbf{T}_{AB}^{GT} \mathbf{P}_A\|^2 + \|\mathbf{T}_{AB}^{-1} \mathbf{P}_B - \mathbf{T}_{AB}^{GT-1} \mathbf{P}_B\|^2 \quad (16)$$

Direct Correspondence Loss. While the Point Displacement Loss best describes errors seen at inference time, it can lead to correspondences that are inaccurate but whose errors average to the correct pose. To improve these errors we directly supervise the learned correspondences $\tilde{\mathbf{V}}_A$ and $\tilde{\mathbf{V}}_B$:

$$\mathcal{L}_{\text{corr}} = \|\tilde{\mathbf{V}}_A - \mathbf{T}_{AB}^{GT} \mathbf{P}_A\|^2 + \|\tilde{\mathbf{V}}_B - \mathbf{T}_{AB}^{GT-1} \mathbf{P}_B\|^2. \quad (17)$$

Correspondence Consistency Loss. Furthermore, a consistency loss can be used. This loss penalizes correspondences that deviate from the final predicted transform. A benefit of this loss is that it

can help the network learn to respect the rigidity of the object, while it is still learning to accurately place the object. Note, that this is similar to the Direct Correspondence Loss, but uses the predicted transform as opposed to the ground truth one. As such, this loss requires no ground truth:

$$\mathcal{L}_{\text{cons}} = \left\| \tilde{\mathbf{V}}_{\mathcal{A}} - \mathbf{T}_{\mathcal{AB}} \mathbf{P}_{\mathcal{A}} \right\|^2 + \left\| \tilde{\mathbf{V}}_{\mathcal{B}} - \mathbf{T}_{\mathcal{AB}}^{-1} \mathbf{P}_{\mathcal{B}} \right\|^2. \quad (18)$$

Overall Training Procedure. We train with a combined loss $\mathcal{L}_{\text{net}} = \mathcal{L}_{\text{disp}} + \lambda_1 \mathcal{L}_{\text{corr}} + \lambda_2 \mathcal{L}_{\text{cons}}$, where λ_1 and λ_2 are hyperparameters. We use a similar network architecture as DCP [26], which consists of DGCNN [47] and a Transformer [28].

In order to quickly adapt to new tasks, we optionally pre-train the DGCNN embedding networks over a large set of individual objects using the InfoNCE loss [48] with a geometric distance weighting and random transformations, to learn $SE(3)$ invariant embeddings, see Appendix E.2 for details.

E.2 Pretraining

We utilize pretraining for the embedding network for the mug hanging task, and describe the details below.

We pretrain embedding network for each object category (mug, rack, gripper), such that the embedding network is $SE(3)$ invariant with respect to the point clouds of that specific object category. Specifically, the mug-specific embedding network is pretrained on 200 ShapeNet [49] mug instances, while the rack-specific and gripper-specific embedding network is trained on the same rack and Franka gripper used at test time, respectively. Note that before our pretraining, the network is randomly initialized with the Kaiming initialization scheme [50]; we don’t adopt any third-party pretrained models.

For the network to be trained to be $SE(3)$ invariant, we pre-train with InfoNCE loss [48] with a geometric distance weighting and random $SE(3)$ transformations. Specifically, given a point cloud of an object instance, $\mathbf{P}_{\mathcal{A}}$, of a specific object category \mathcal{A} , and an embedding network $g_{\mathcal{A}}$, we define the point-wise embedding for $\mathbf{P}_{\mathcal{A}}$ as $\Phi_{\mathcal{A}} = g_{\mathcal{A}}(\mathbf{P}_{\mathcal{A}})$, where $\phi_i^{\mathcal{A}} \in \Phi_{\mathcal{A}}$ is a d -dimensional vector for each point $p_i^{\mathcal{A}} \in \mathbf{P}_{\mathcal{A}}$. Given a random $SE(3)$ transformation, \mathbf{T} , we define $\Psi_{\mathcal{A}} = g_{\mathcal{A}}(\mathbf{T}\mathbf{P}_{\mathcal{A}})$, where $\psi_i^{\mathcal{A}} \in \Psi_{\mathcal{A}}$ is the d -dimensional vector for the i th point $p_i^{\mathcal{A}} \in \mathbf{P}_{\mathcal{A}}$.

The weighted contrastive loss used for pretraining, \mathcal{L}_{wc} , is defined as

$$\mathcal{L}_{wc} := - \sum_i \log \left[\frac{\exp(\phi_i^{\mathcal{A}\top} \psi_i)}{\sum_j \exp(d_{ij}(\phi_i^{\mathcal{A}\top} \psi_j))} \right] \quad (19)$$

$$d_{ij} := \begin{cases} \frac{1}{\mu} \tanh(\lambda \|p_i^{\mathcal{A}} - p_j^{\mathcal{A}}\|_2), & \text{if } i \neq j \\ 1, & \text{otherwise} \end{cases} \quad (20)$$

$$\mu := \max(\tanh(\lambda \|p_i^{\mathcal{A}} - p_j^{\mathcal{A}}\|_2)) \quad (21)$$

For this pretraining, we use $\lambda := 10$.

E.3 Architectural Variants

Goal-Conditioned TAX-Pose: To enable a single TAX-Pose model to scale to multiple related placement sub-tasks for a pair of action and anchor objects, we design a **goal-conditioned** variant (**TAX-Pose GC**), which receives a one-hot encoding of the desired semantic goal position (e.g. ‘top’, ‘left’, ...) for the task. This contextual encoding is incorporated into each DGCNN module in the same way as proposed in the original DGCNN paper. This encoding can be used to provide an embedding of the specific placement relationship that is desired in a scene (e.g. selecting a ‘top’ vs. ‘left’ placement position) and thus enable goal conditioned placement.

Vector Neurons: We briefly experimented with Vector Neurons [51] and found that this led to worse performance on this task.

F Additional Results

F.1 NDF Placement Tasks

F.1.1 Further Ablations on Mug Hanging Task

In order to examine the effects of different design choices in the training pipeline, we conduct ablation experiments with final task-success (*grasp*, *place*, *overall*) as evaluation metrics for Mug Hanging task with upright pose initialization for the following components of our method, see Table 6 for full ablation results along six ablated dimensions as detailed below. We also performed an ablation experiment on alternative cross-object attention weight computation, as explained in Appendix C and results can be found in Table 5. For consistency, all ablated models are trained for 15K steps.

1. **Loss.** In the full pipeline reported, we use a weighted sum of the three types of losses described in Section 4.2 of the paper. Specifically, the loss used \mathcal{L}_{net} is given by

$$\mathcal{L}_{\text{net}} = \mathcal{L}_{\text{disp}} + \lambda_1 \mathcal{L}_{\text{cons}} + \lambda_2 \mathcal{L}_{\text{corr}} \quad (22)$$

where we chose $\lambda_1 = 0.1$, $\lambda_2 = 1$ after hyperparameter search.

We ablate usage of all three types of losses, by reporting the final task performance in simulation for all experiments, specifically, we report task success on the following \mathcal{L}_{net} variants.

- (a) Remove the point displacement loss term, $\mathcal{L}_{\text{disp}}$, after which we are left with

$$\mathcal{L}'_{\text{net}} = (0.1)\mathcal{L}_{\text{cons}} + \mathcal{L}_{\text{corr}}$$

- (b) Remove the direct correspondence loss term, $\mathcal{L}_{\text{corr}}$, after which we are left with

$$\mathcal{L}'_{\text{net}} = \mathcal{L}_{\text{disp}} + (0.1)\mathcal{L}_{\text{cons}}$$

- (c) Remove the correspondence consistency loss term, $\mathcal{L}_{\text{cons}}$, after which we are left with

$$\mathcal{L}'_{\text{net}} = \mathcal{L}_{\text{disp}} + \mathcal{L}_{\text{corr}}$$

- (d) From testing loss variants above, we found that the point displacement loss is a vital contributing factor for task success, where removing this loss term results in no overall task success, as shown in Table 6. However, in practice, we have found that adding the correspondence consistency loss and direct correspondence loss generally help to lower the rotational error of predicted placement pose compared to the ground truth of collected demos. To further investigate the effects of the combination of these two loss terms, we used a scaled weighted combination of $\mathcal{L}_{\text{cons}}$ and $\mathcal{L}_{\text{corr}}$, such that the former weight of the displacement loss term is transferred to consistency loss term, with the new $\lambda_1 = 1.1$, and with $\lambda_2 = 1$ stays unchanged. Note that this is different from variant (a) above, as now the consistency loss given a comparable weight with dense correspondence loss term, which intuitively makes sense as the consistency loss is a function of the predicted transform $\mathbf{T}_{\mathcal{A}\mathcal{B}}$ to be used, while the dense correspondence loss is instead a function of the ground truth transform, $\mathbf{T}_{\mathcal{A}\mathcal{B}}^{\text{GT}}$, which provides a less direct supervision on the predicted transforms. Thus we are left with

$$\mathcal{L}'_{\text{net}} = (1.1)\mathcal{L}_{\text{cons}} + \mathcal{L}_{\text{corr}}$$

2. **Usage of Correspondence Residuals.** After predicting a per-point soft correspondence between objects \mathcal{A} and \mathcal{B} , we adjust the location of the predicted corresponding points by further predicting a point-wise correspondence residual vector to displace each of the predicted corresponding point. This allows the predicted corresponding point to get mapped to free space outside of the convex hulls of points in object \mathcal{A} and \mathcal{B} . This is a desirable adjustment for mug hanging task, as the desirable cross-pose usually require points on the mug handle to be placed somewhere near but not in contact with the mug rack, which can be outside of the convex hull of rack points. We ablate correspondence residuals by directly using the soft correspondence prediction to find the cross-pose transform through weighted SVD, without any correspondence adjustment via correspondence residual.

3. **Weighted SVD vs Non-weighted SVD.** We leverage weighted SVD as described in **Section 4.1** of the paper as we leverage predicted per-point weight to signify the importance of specific correspondence. We ablate the use of weighted SVD, and we use an un-weighted SVD, where instead of using the predicted weights, each correspondence is assign equal weights of $\frac{1}{N}$, where N is the number of points in the point cloud \mathbf{P} used.
4. **Pretraining.** In our full pipeline, we pretrain the point cloud embedding network such that the embedding network is $SE(3)$ invariant. Specifically, the mug-specific embedding network is pretrained on 200 ShapeNet mug objects, while the rack-specific and gripper specific embedding network is trained on the same rack and Franka gripper used at test time, respectively. We conduct ablation experiments where
 - (a) We omit the pretraining phase of embedding network
 - (b) We do not finetune the embedding network during downstream training with task-specific demonstrations.

Note that in practice, we find that pretraining helps speed up the downstream training by about a factor of 3, while models with or without pretraining both reach a similar final performance in terms of task success after both models converge.
5. **Usage of Transformer as Cross-object Attention Module.** In the full pipeline, we use transformer as the cross-object attention module, and we ablate this design choice by replacing the transformer architecture with a simple 3-layer MLP with ReLU activation and hidden dimension of 256, and found that this leads to worse place and grasp success.
6. **Dimension of Embedding.** In the full pipeline, the embedding is chosen to be of dimension 512. We conduct experiment on much lower dimension of 16, and found that with dimension =16, the place success is much lower, dropped from 0.97 to 0.59.

Ablation Experiment	Grasp	Place	Overall
No $\mathcal{L}_{\text{disp}}$	0.01	0	0
No $\mathcal{L}_{\text{corr}}$	0.89	0.91	0.84
No $\mathcal{L}_{\text{cons}}$	0.99	0.95	0.94
Scaled Combination: $1.1\mathcal{L}_{\text{cons}} + \mathcal{L}_{\text{corr}}$	0.10	0.01	0.01
No Adjustment via Correspondence Residuals	0.97	0.96	0.93
Unweighted SVD	0.92	0.94	0.88
No Finetuning for Embedding Network	0.98	0.93	0.91
No Pretraining for Embedding Network	0.99	0.72	0.71
3-Layer MLP In Place of Transformer	0.90	0.82	0.76
Embedding Network Feature Dim = 16	0.98	0.59	0.57
TAX-Pose (Ours)	0.99	0.97	0.96

Table 6: Mug Hanging Ablations Results

F.1.2 Effects of Pretraining on Mug Hanging Task

We explore the effects of pretraining on the final task performance, as well as training convergence speed. We have found that pretraining the point cloud embedding network as described in E.2, is a helpful but not necessary component in our training pipeline. Specifically, we find that while utilizing pretraining reduces training time, allowing the model to reach similar task performance and train rotation/translation error with much fewer training steps, this component is not necessary if training time is not of concern. In fact, as see in Table 7, we find that for mug hanging tasks, by training the models from scratch without our pretraining, the models are able to reach similar level of task performance of 0.99 grasp, 0.92 for place and 0.92 for overall success rate. Furthermore, it is able to achieve similar level of train rotation error of 4.91° and translation error of $0.01m$, compared

to the models with pretraining. However, without pre-training, the model needs to be trained for about 2 times longer (26K steps compared to 15K steps) to reach the similar level of performance. Thus we adopt our object-level pretraining in our overall pipeline to allow lower training time.

Another benefit of pretraining is that the pretraining for each object category is done in a task-agnostic way, so the network can be more quickly adapted to new tasks after the pretraining is performed. For example, we use the same pre-trained mug embeddings for both the gripper-mug cross-pose estimation for grasping as well as the mug-rack cross-pose estimation for mug hanging.

Ablation Experiment	Grasp	Place	Overall	Train Rotation Error ($^{\circ}$)	Train Translation Error (m)
No Pre-Training for Embedding Network (trained for 26K steps)	0.99	0.92	0.92	4.91	0.01
No Pre-Training for Embedding Network (trained for 15K steps)	0.99	0.72	0.71	15.39	0.01
TAX-Pose (Ours) (trained for 15K steps)	0.99	0.97	0.96	4.33	0.01

Table 7: Ablation Experiments on the Effects of Pre-Training. We report the task success rate for upright mug hanging task over 100 trials each, as well as the grasping model’s training rotational error ($^{\circ}$) and translation error (m).

F.1.3 Additional Simulation Experiments on Bowl and Bottle Placement Task

Object	Algorithm	Grasp	Place	Overall	Grasp	Place	Overall
		Upright Pose			Arbitrary Pose		
Mug	DON [12]	0.91	0.50	0.45	0.35	0.45	0.17
	NDF [14]	0.96	0.92	0.88	0.78	0.75	0.58
	TAX-Pose (Ours)	0.99	0.97	0.96	0.75	0.84	0.63
Bowl	DON [12]	0.50	0.35	0.11	0.08	0.20	0
	NDF [14]	0.91	1	0.91	0.79	0.97	0.78
	TAX-Pose (Ours)	0.99	0.92	0.92	0.74	0.85	0.85
Bottle	DON [12]	0.79	0.24	0.24	0.05	0.02	0.01
	NDF [14]	0.87	1	0.87	0.78	0.99	0.77
	TAX-Pose (Ours)	0.55	0.99	0.55	0.61	0.55	0.52

Table 8: Unseen Object Instance Manipulation Task Success Rates (\uparrow) in Simulation on *Mug*, *Bowl* and *Bottle* for Upright and Arbitrary Initial Pose. Each result is the success rate over 100 trials.

Additional results on *Grasp*, *Place* and *Overall* success rate in simulation for **Bowl** and **Bottle** are shown in Table 8. For bottle and bowl experiment, we follow the same experimentation setup as in [14], where the successful *grasp* is considered if a stable grasp of the object is obtained, and a successful *place* is considered when the bottle or bowl is stably placed upright on the elevated flat slab over the table without falling on the table. Reported task success results in are for both *Upright Pose* and *Arbitrary Pose* run over 100 trials each.

Unlike mugs, bowls and bottles exhibit rotational object symmetry, which we have found cause the trained model to perform poorly in the *Grasp* task. To mitigate this, we applied symmetry breaking techniques for the **Bowl** and **Bottle** placement tasks by algorithmically creating symmetry labels, $l_i^{\mathcal{K}} \in [-1, 1]$ for object \mathcal{K} , as continuous real numbers between -1 and 1 inclusive for each point $\mathbf{p}_i^{\mathcal{K}}$ during training and testing. The symmetry label for i -th point is concatenated with the associated point-wise embedding, $\psi_i^{\mathcal{K}}$, resulting in an augmented point-wise embedding, $\hat{\psi}_i^{\mathcal{K}} := [\psi_i^{\mathcal{K}} \ l_i^{\mathcal{K}}]^{\top} \in \mathbb{R}^{d+1}$, which is then passed into the Cross-Correspondence Estimators. The input layer of these estimators are modified to account for the corresponding new input dimension.

The symmetry labels for each object are generated using an easily computed bisecting plane. Given segmented point cloud demonstration of the gripper and the bottle/bowl in goal configuration, we apply Principle Component Analysis (PCA) to the individual object point cloud of the gripper and bottle/bowl.

The symmetry labels for the gripper are defined using the PCA vector with largest principal component positioned at the gripper point cloud centroid, $\hat{\mathbf{s}}_{gripper}$. This vector defines the plane that bisects the gripper along its axis of actuation.

For each point $\mathbf{p}_i^{gripper}$ in the gripper point cloud, compute the unit vector between it and gripper centroid $\mu_{gripper}$,

$$\hat{\mathbf{v}}_i^{gripper} = \frac{\mathbf{p}_i^{gripper} - \mu_{gripper}}{\|\mathbf{p}_i^{gripper} - \mu_{gripper}\|}, \quad (23)$$

and retrieve the symmetry labels as the dot-product between the unit vectors,

$$l_i^{gripper} = \langle \mathbf{s}_{gripper}, \hat{\mathbf{v}}_i^{gripper} \rangle. \quad (24)$$

To compute the symmetry labels for the bottle/bowl point clouds at training time, we retrieve the rotational symmetry axis, $\hat{\mathbf{v}}_{rot}$ of the bottle/bowl (pointing upward towards the bottle/bowl opening) using PCA. This vector is the largest principal component for the bottles and the smallest component for the bowls. We define a bisecting plane using both this symmetry axis, as well as the normalized vector pointing from the centroid of bottle/bowl to the centroid of the gripper, $\hat{\mathbf{v}}_{gripper}$. For the bottle points, the normal of the bisecting plane is found using the normalized cross-product of these two vectors,

$$\mathbf{s}_{bottle} = \frac{\hat{\mathbf{v}}_{rot} \times \hat{\mathbf{v}}_{gripper}}{\|\hat{\mathbf{v}}_{rot} \times \hat{\mathbf{v}}_{gripper}\|}, \quad (25)$$

which separates the bottle into left and right sides with respect to the gripper. For the bowl points, we orthogonalize the gripper vector, $\hat{\mathbf{v}}_{gripper}$ to symmetry vector, $\hat{\mathbf{v}}_{rot}$,

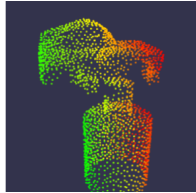
$$\mathbf{s}_{bowl} = \frac{\hat{\mathbf{v}}_{gripper} - \langle \hat{\mathbf{v}}_{gripper}, \hat{\mathbf{v}}_{rot} \rangle \hat{\mathbf{v}}_{rot}}{\|\hat{\mathbf{v}}_{gripper} - \langle \hat{\mathbf{v}}_{gripper}, \hat{\mathbf{v}}_{rot} \rangle \hat{\mathbf{v}}_{rot}\|}. \quad (26)$$

This results in a bisecting plane that separates the bowl into a near and far half with respect to the gripper. Similar to the gripper symmetry labels, the symmetry labels for the bottle/bowl are computed using the normalized vector between each bottle/bowl point and the bottle/bowl centroid, $\hat{\mathbf{v}}_i^{\{bottle, bowl\}}$,

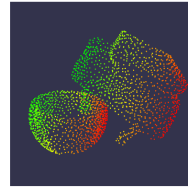
$$l_i^{\{bottle, bowl\}} = \langle \mathbf{s}_{\{bottle, bowl\}}, \hat{\mathbf{v}}_i^{\{bottle, bowl\}} \rangle. \quad (27)$$

At inference, instead of using the gripper location to compute $\mathbf{v}_{gripper}$ for the bottle and bowl labels, we use a random vector perpendicular to \mathbf{v}_{rot} . This allows us to use semantically meaningful symmetry labels at training time, and then arbitrarily break the symmetry at test time.

See Figure 9a and 9b for visualization of symmetry labels obtained from aforementioned procedures, where the color spectrum of red represents symmetry labels of 1, and green represents -1.



(a) Symmetry labels for bottle and gripper



(b) Symmetry labels for bowl and gripper

F.1.4 Failure Cases

Some failure cases for TAX-Pose occur when the predicted gripper misses the rim of the mug by a xy-plane translation error, thus resulting in failure of grasp, as seen in Figure 10a. A common failure mode for the mug placement subtask is characterized by an erroneous transform prediction

that results in the mug’s handle completely missing the rack hanger, thus resulting in placement failure, as seen in Figure 10b.

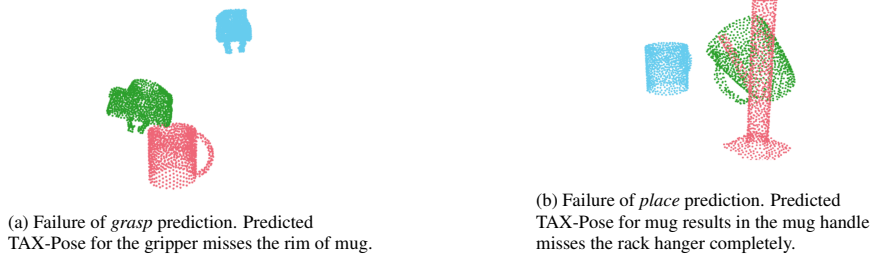


Figure 10: An illustration of unsuccessful TAX-Pose predictions for mug hanging. In both subfigures, red points represent the anchor object, blue points represent action object’s starting pose, and green points represent action object’s predicted pose.

F.2 PartNet-Mobility Tasks

F.2.1 Expanded Results Tables

In the main text, we presented aggregated results of the performance of each method by averaging the quantitative metrics for each sub-task for each object (“In”, “On”, “Left”, and “Right” in simulation and “In”, “On” and “Left” in real-world), and then averaged across object classes to arrive at a single metric per method. Here, we present the per-class breakdown of performance. See Table 9 for simulated results, and Table 10 for real-world results.

		AVG.																	
		\mathcal{E}_R	\mathcal{E}_t	\mathcal{E}_R	\mathcal{E}_t	\mathcal{E}_R	\mathcal{E}_t	\mathcal{E}_R	\mathcal{E}_t	\mathcal{E}_R	\mathcal{E}_t	\mathcal{E}_R	\mathcal{E}_t	\mathcal{E}_R	\mathcal{E}_t	\mathcal{E}_R	\mathcal{E}_t	\mathcal{E}_R	\mathcal{E}_t
Baselines	E2E BC	42.26	0.73	37.82	0.82	37.15	0.65	44.84	0.68	30.69	1.06	40.38	0.69	45.09	0.76	45.00	0.79	45.65	0.64
	E2E DAgger [52]	37.96	0.69	34.15	0.76	36.61	0.66	40.91	0.65	24.87	0.97	35.95	0.70	40.34	0.74	32.86	0.79	39.45	0.53
Ablations	Traj. Flow [53]	35.95	0.67	31.24	0.82	39.21	0.72	34.35	0.66	28.48	0.75	37.14	0.59	29.49	0.70	39.60	0.76	39.69	0.48
	Goal Flow [53]	26.64	0.17	25.88	0.15	25.05	0.15	30.62	0.15	27.61	0.10	28.01	0.18	20.96	0.24	29.02	0.23	22.13	0.20
Ours	TAX-Pose	6.64	0.16	6.85	0.16	2.05	0.10	3.87	0.12	4.04	0.08	12.71	0.31	6.87	0.37	5.89	0.13	14.93	0.18
	TAX-Pose GC	4.94	0.16	6.18	0.16	1.75	0.10	2.94	0.10	3.02	0.06	10.15	0.27	6.93	0.35	3.76	0.11	4.76	0.11

Table 9: Goal Inference Rotational and Translational Error Results (\downarrow). Rotational errors (\mathcal{E}_R) are in degrees ($^\circ$) and translational errors (\mathcal{E}_t) are in meters (m). The lower the better.

	In			On			Left		
Goal Flow	0.00	0.10	0.30	0.05	N/A	0.20	0.50	0.65	0.60
TAX-Pose	1.00	1.00	0.85	1.00	N/A	1.00	0.85	0.90	0.70

Table 10: Combined per-task results for real-world goal placement success rate.

We further provide results per-sub-task in simulation. For each category of anchor objects, sub-tasks may or may not all be well-defined. For example, the doors of safes might occlude the action object completely in a demonstration for “Left” and “Right” tasks due to the handedness of the door; and a table’s height might be too tall for the camera to see the action object placed during the “Top” task. To avoid these ill-defined cases, we omit object-category / sub-task pairings which cannot be consistently defined from training and evaluation. We show visualizations of each defined task for each object category in Figure 11. Results for each sub-task can be found in Tables 11⁴, 12, 13, and 14 respectively.

⁴Categories from left to right: microwave, dishwasher, oven, fridge, table, washing machine, safe, drawer.

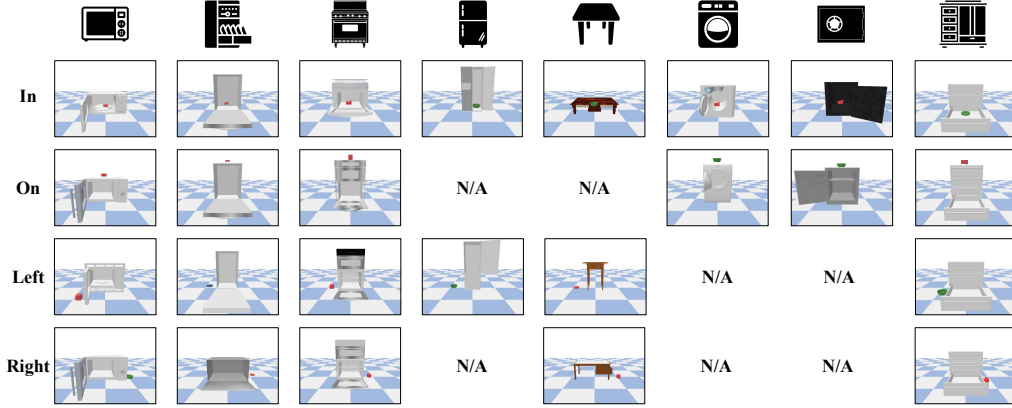


Figure 11: A visualization of all categories of anchor objects and associated semantic tasks, with action objects in ground-truth TAX-Poses used in simulation training.

		AVG.																	
		\mathcal{E}_R	\mathcal{E}_t	\mathcal{E}_R	\mathcal{E}_t	\mathcal{E}_R	\mathcal{E}_t	\mathcal{E}_R	\mathcal{E}_t	\mathcal{E}_R	\mathcal{E}_t	\mathcal{E}_R	\mathcal{E}_t						
Baselines	E2E BC	42.37	0.69	40.49	0.80	50.79	0.59	48.02	0.61	30.69	1.09	36.59	0.81	48.48	0.42	41.42	0.84	42.49	0.37
	E2E DAgger [52]	36.06	0.67	38.57	0.68	43.99	0.63	42.34	0.57	24.87	0.96	30.87	0.90	42.96	0.46	29.79	0.83	35.08	0.33
Ablations	Traj. Flow [53]	34.48	0.65	35.39	0.85	43.42	0.63	35.51	0.60	28.26	0.80	27.67	0.68	25.91	0.44	43.59	0.82	36.05	0.36
	Goal Flow [53]	27.49	0.21	25.41	0.08	31.07	0.13	27.05	0.27	27.80	0.11	29.02	0.38	19.22	0.36	31.56	0.18	28.81	0.19
Ours	TAX-Pose	11.74	0.23	5.81	0.11	1.82	0.08	5.92	0.11	3.67	0.07	19.54	0.41	7.96	0.63	5.96	0.12	43.27	0.33

Table 11: Goal Inference Rotational and Translational Error Results (\downarrow) for the “In” Goal. Rotational errors (\mathcal{E}_R) are in degrees ($^\circ$) and translational errors (\mathcal{E}_t) are in meters (m). The lower the better.

		AVG.													
		\mathcal{E}_R	\mathcal{E}_t	\mathcal{E}_R	\mathcal{E}_t	\mathcal{E}_R	\mathcal{E}_t	\mathcal{E}_R	\mathcal{E}_t	\mathcal{E}_R	\mathcal{E}_t				
Baselines	E2E BC	42.69	0.74	41.94	0.74	36.70	0.52	38.23	0.73	41.69	1.10	48.57	0.75	48.98	0.63
	E2E DAgger [52]	37.68	0.70	39.24	0.69	31.63	0.54	41.06	0.68	37.72	1.03	35.94	0.75	40.47	0.51
Ablations	Traj. Flow [53]	35.13	0.76	34.78	0.70	39.14	0.59	31.10	0.69	33.07	0.97	35.61	0.71	37.09	0.87
	Goal Flow [53]	22.10	0.20	27.82	0.26	20.43	0.09	34.66	0.10	22.71	0.12	26.48	0.27	0.48	0.32
Ours	TAX-Pose	4.45	0.12	4.21	0.12	2.29	0.10	2.73	0.09	5.77	0.10	5.81	0.13	5.89	0.19

Table 12: Goal Inference Rotational and Translational Error Results (\downarrow) for the “On” Goal. Rotational errors (\mathcal{E}_R) are in degrees ($^\circ$) and translational errors (\mathcal{E}_t) are in meters (m). The lower the better.

		AVG.													
		\mathcal{E}_R	\mathcal{E}_t	\mathcal{E}_R	\mathcal{E}_t	\mathcal{E}_R	\mathcal{E}_t	\mathcal{E}_R	\mathcal{E}_t	\mathcal{E}_R	\mathcal{E}_t				
Baselines	E2E BC	44.87	0.74	30.95	0.89	36.86	0.72	56.86	0.52	34.35	1.03	31.69	0.77	46.86	0.78
	E2E DAgger [52]	41.32	0.68	31.40	0.84	38.49	0.73	47.64	0.51	36.47	0.99	27.72	0.73	39.83	0.51
Ablations	Traj. Flow [53]	38.85	0.58	31.87	1.07	39.48	0.44	39.48	0.44	28.71	0.69	41.06	0.73	40.70	0.31
	Goal Flow [53]	29.64	0.10	28.51	0.10	26.33	0.08	32.96	0.07	27.42	0.10	22.04	0.09	27.42	0.15
Ours	TAX-Pose	6.02	0.17	12.73	0.28	1.59	0.11	2.91	0.12	4.41	0.08	12.12	0.34	6.38	0.12

Table 13: Goal Inference Rotational and Translational Error Results (\downarrow) for the “Left” Goal. Rotational errors (\mathcal{E}_R) are in degrees ($^\circ$) and translational errors (\mathcal{E}_t) are in meters (m). The lower the better.






		AVG.											
		\mathcal{E}_R	\mathcal{E}_t	\mathcal{E}_R	\mathcal{E}_t	\mathcal{E}_R	\mathcal{E}_t	\mathcal{E}_R	\mathcal{E}_t				
Baselines	E2E BC	39.11	0.76	37.89	0.86	24.26	0.77	36.27	0.88	52.86	0.48	44.26	0.78
	E2E DAgger [52]	36.80	0.73	27.40	0.84	32.31	0.74	32.61	0.82	49.27	0.46	42.40	0.78
Ablations	Traj. Flow [53]	35.33	0.71	22.93	0.66	34.78	1.22	31.29	0.92	42.71	0.37	44.93	0.36
	Goal Flow [53]	27.34	0.16	21.79	0.15	22.37	0.28	27.79	0.15	32.96	0.07	31.79	0.15
Ours	TAX-Pose	4.33	0.13	4.64	0.14	2.48	0.11	3.91	0.15	6.47	0.17	4.17	0.08

Table 14: Goal Inference Rotational and Translational Error Results (\downarrow) for the “Right” Goal. Rotational errors (\mathcal{E}_R) are in degrees ($^\circ$) and translational errors (\mathcal{E}_t) are in meters (m). The lower the better.

F.2.2 Goal-Conditioned Variant

We train our goal-conditioned variant **TAX-Pose GC** (Appendix E.3) to predict the correct cross-pose across sub-tasks, incorporating a one-hot encoding of each sub-task (i.e. ‘top’, ‘in’, ‘left’, ‘right’) so the model can infer the desired semantic goal location. Importantly, as with the task-specific model (**TAX-Pose**), the **TAX-Pose GC** model is trained across **all PartNet-Mobility object categories**. We report the performance of the variants in Table 9.

F.2.3 Failure Cases

Some failure cases for TAX-Pose occur when the predicted cross-pose does not respect the physical constraints in the scene. For example, as seen in Fig. 12. TAX-Pose would fail when the prediction violates the physical constraints of the objects, which in this case the action object collides with the anchor object. In the real world, this would yield the robot unable to plan a correct path.

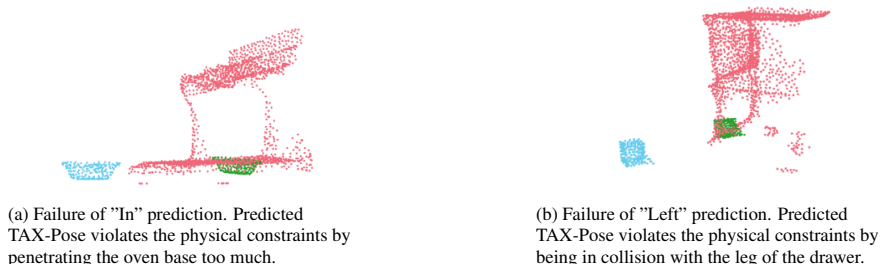


Figure 12: An illustration of unsuccessful real-world TAX-Pose predictions. In both subfigures, red points represent the anchor object, blue points represent action object’s starting pose, and green points represent action object’s predicted pose.

G Task Details

G.1 NDF Task Details

In this section, we describe the Mug Hanging task of the NDF Tasks and experiments in detail. The Mug Hanging task is consisted of two sub tasks: *grasp* and *place*. A *grasp* success is achieved when the mug is grasped stably by the gripper, while a *place* success is achieved when the mug is hung stably on the hanger of the rack. Overall mug hanging success is achieved when the predicted transforms enable both grasp and place success for the same trial. See Figure 13 for a detailed breakdown of the mug hanging task in stages.

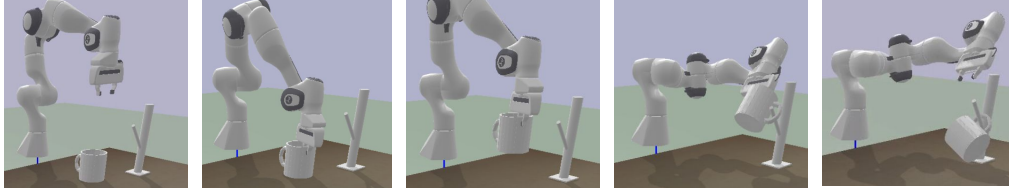


Figure 13: Visualization of Mug Hanging Task (Upright Pose). Mug hanging task is consisted of two stages, given a mug that is randomly initialized on the table, the model first predicts a $SE(3)$ transform from gripper end effector to the mug rim $\mathbf{T}_{g \rightarrow m}$, then grasp it by the rim. Next, the model predicts another $SE(3)$ transform from the mug to the rack $\mathbf{T}_{m \rightarrow r}$ such that the mug handle gets hanged on the the mug rack.

G.1.1 Baseline Description

In simulation, we compare our method to the results described in [14].

- **Dense Object Nets (DON)** [12]: Using manually labeled semantic keypoints on the demonstration clouds, DON is used to compute sparse correspondences with the test objects. These correspondences are converted to a pose using SVD. A full description of usage of DON for the mug hanging task can be found in [14].
- **Neural Descriptor Field (NDF)** [14]: Using the learned descriptor field for the mug, the positions of a constellation of task specific query points are optimized to best match the demonstration using gradient descent.

G.1.2 Training Data

To be directly comparable with the baselines we compared to, we use the exact same sets of demonstration data used to train the network in NDF [14], where the data are generated via teleoperation in PyBullet, collected on 10 mug instances with random pose initialization.

G.1.3 Training and Inference

Using the pretrained embedding network for mug and gripper, we train a grasping model for the grasping task to predict a transformation $\mathbf{T}_{g \rightarrow m}$ in gripper’s frame from gripper to mug to complete the *grasp* stage of the task. Similarly, using the pretrained embedding network for rack and mug, we train a placement model for the placing task to predict a transformation $\mathbf{T}_{m \rightarrow r}$ in mug’s frame from mug to rack to complete the *place* stage of the task. Both models are trained with the same combined loss \mathcal{L}_{net} as described in the main paper. During inference, we simply use grasping model to predict the $\mathbf{T}_{g \rightarrow m}$ at test time, and placement model to predict $\mathbf{T}_{m \rightarrow r}$ at test time.

G.1.4 Motion Planning

After the model predicts a transformation $\mathbf{T}_{g \rightarrow m}$ and $\mathbf{T}_{m \rightarrow r}$, using the known gripper’s world frame pose, we calculate the desired gripper end effector pose at grasping and placement, and pass the end effector to IKFast to get the desired joint positions of Franka at grasping and placement. Next we pass the desired joint positions at gripper’s initial pose, and desired grasping joint positions to OpenRAVE motion planning library to solve for trajectory from gripper’s initial pose to grasp pose, and then grasp pose to placement pose for the gripper’s end effector.

G.1.5 Real-World Experiments

We pre-train the DGCNN embedding network with rotation-equivariant loss on ShapeNet mugs’ simulated point clouds in simulation. Using the pre-trained embedding, we then train the full TAX-Pose model with the 10 collected real-world point clouds.

G.2 PartNet-Mobility Object Placement Task Details

In this section, we describe the PartNet-Mobility Object Placement experiments in detail. We select a set of household furniture objects from the PartNet-Mobility dataset as the anchor objects, and a set of small rigid objects released with the Ravens simulation environment as the action objects. For each anchor object, we define a set of semantic goal positions (i.e. ‘top’, ‘left’, ‘right’, ‘in’), where action objects should be placed relative to each anchor. Each semantic goal position defines a unique task in our cross-pose prediction framework.

G.2.1 Dataset Preparation

Simulation Setup. We leverage the PartNet-Mobility dataset [35] to find common household objects as the anchor object for TAX-Pose prediction. The selected subset of the dataset contains 8 categories of objects. We split the objects into 54 seen and 14 unseen instances. During training, for a specific task of each of the seen objects, we generate an action-anchor objects pair by randomly sampling transformations from $SE(3)$ as cross-poses. The action object is chosen from the Ravens simulator’s rigid body objects dataset [54]. We define a subset of four tasks (“In”, “On”, “Left” and “Right”) for each selected anchor object. Thus, there exists a ground-truth cross-pose (defined by human manually) associated with each defined specific task. We then use the ground-truth TAX-Poses to supervise each task’s TAX-Pose prediction model. For each observation action-anchor objects pair, we sample 100 times using the aforementioned procedure for the training and testing datasets.

Real-World Setup. In real-world, we select a set of anchor objects: Drawer, Fridge, and Oven and a set of action objects: Block and Bowl. We test 3 (“In”, “On”, and “Left”) TAX-Pose models in real-world without retraining or finetuning. The point here is to show the method capability of generalizing to unseen real-world objects.

G.2.2 Metrics

Simulation Metrics. In simulation, with access to the object’s ground-truth pose, we are able to quantitatively calculate translational and rotation error of the TAX-Pose prediction models. Thus, we report the following metrics on a held-out set of anchor objects in simulation:

Translational Error: The L2 distance between the inferred cross-pose translation ($\mathbf{t}_{AB}^{\text{pred}}$) and the ground-truth pose translation ($\mathbf{t}_{AB}^{\text{GT}}$).

Rotational Error: The geodesic $SO(3)$ distance [42, 43] between the predicted cross-pose rotation ($\mathbf{R}_{AB}^{\text{pred}}$) and the ground-truth rotation ($\mathbf{R}_{AB}^{\text{GT}}$).

$$\mathcal{E}_t = \|\mathbf{t}_{AB}^{\text{pred}} - \mathbf{t}_{AB}^{\text{GT}}\|_2 \qquad \mathcal{E}_R = \frac{1}{2} \arccos \left(\frac{\text{tr}(\mathbf{R}_{AB}^{\text{pred}\top} \mathbf{R}_{AB}^{\text{GT}}) - 1}{2} \right)$$

Real-World Metrics. In real-world, due to the difficulty of defining ground-truth TAX-Pose, we instead manually, qualitatively define goal “regions” for each of the anchor-action pairs. The goal-region should have the following properties:

- The predicted TAX-Pose of the action object should appear visually correct. For example, if the specified task is “In”, then the action object should be indeed contained within the anchor object after being transformed by predicted TAX-Pose.
- The predicted TAX-Pose of the action object should not violate physical constraints of the workspace and of the relation between the action and anchor objects. Specifically, the action object should not interfere with/collide with the anchor object after being transformed by the predicted TAX-Pose. See Figure 12 for an illustration of TAX-Pose predictions that fail to meet this criterion.

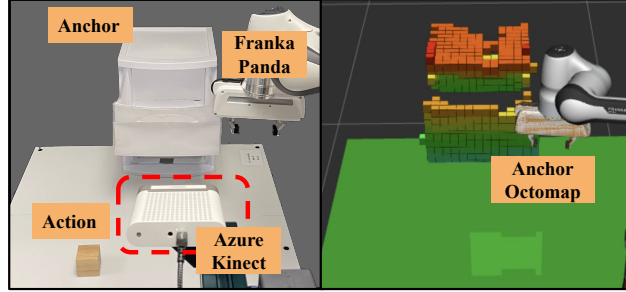


Figure 14: Real-world experiments illustration. **Left:** work-space setup for physical experiments. **Center:** Octomap visualization of the perceived anchor object.

G.2.3 Motion Planning

In both simulated and real-world experiments, we use off-the-shelf motion-planning tools to find a path between the starting pose and goal pose of the action object.

Simulation. To actuate the action object from its starting pose \mathbf{T}_0 to its goal pose transformed by the predicted TAX-Pose $\hat{\mathbf{T}}_{AB}\mathbf{T}_0$, we plan a path free of collision. Learning-based methods such as [55] deal with collision checking with point clouds by training a collision classifier. A more data-efficient method is by leveraging computer graphics techniques, transforming the point clouds into marching cubes [56], which can then be used to efficiently reconstruct meshes. Once the triangular meshes are reconstructed, we can deploy off-the-shelf collision checking methods such as FCL [57] to detect collisions in the planned path. Thus, in our case, we use position control to plan a trajectory of the action object \mathcal{A} to move it from its starting pose to the predicted goal pose. We use OMPL [58] as the motion planning tool and the constraint function passed into the motion planner is from the output of FCL after converting the point clouds to meshes via marching cubes.

Real World. In real-world experiments, we need to resolve several practical issues to make TAX-Pose prediction model viable. First, we do not have access to a mask that labels action and anchor objects. Thus, we manually define a mask by using a threshold value of y -coordinate to automatically detect discontinuity in y -coordinates, representing the gap of spacing between action and anchor objects upon placement. Next, grasping action objects is a non-trivial task. Since, we are only using 2 action objects (a cube and a bowl), we manually define a grasping primitive for each action object. This is done by hand-picking an offset from the centroid of the action object before grasping, and an approach direction after the robot reaches the pre-grasp pose to make contacts with the object of interest. The offsets are chosen via kinesthetic teaching on the robot when the action object is under identity rotation (canonical pose). Finally, we need to make an estimation of the action’s starting pose for motion planning. This is done by first statistically cleaning the point cloud [53] of the action object, and then calculating the centroid of the action object point cloud as the starting position. For starting rotation, we make sure the range of the rotation is not too large for the pre-defined grasping primitive to handle. Another implementation choice here is to use ICP [18] calculate a transformation between the current point cloud to a pre-scanned point cloud in canonical (identity) pose. We use the estimated starting pose to guide the pre-defined grasp primitive. Once a successful grasp is made, the robot end-effector is rigidly attached to the action object, and we can then use the same predicted TAX-Pose to calculate the end pose of the robot end effector, and thus feed the two poses into MoveIt! to get a full trajectory in joint space. Note here that the collision function in motion planning is comprised of two parts: workspace and anchor object. That is, we first reconstruct the workspace using boxes to avoid collision with the table top and camera mount, and we then reconstruct the anchor object in RViz using Octomap [59] using the cleaned anchor object point cloud. In this way, the robot is able to avoid collision with the anchor object as well. See Figure 14 for the workspace.

G.2.4 Baselines Description

In simulation, we compare our method to a variety of baseline methods.

- **E2E Behavioral Cloning:** Generate motion-planned trajectories using OMPL that take the action object from start to goal. These serve as “expert” trajectories for Behavioral Cloning (BC). Our policy is represented as a PointNet++ [60] network that, at each time step, takes as input the point cloud observation of the action and anchor objects and outputs an incremental 6-DOF transformation that imitates the expert trajectory. The 6-DoF transformation is expressed using Euclidean xyz translation and rotation quaternion. The final achieved pose of the action object at the terminal state is used for computing the evaluation metrics.
- **E2E DAgger:** Using the same BC dataset and the same PointNet++ [60] architecture as above, we train a policy that outputs the same transformation representation as in BC using DAgger [52]. The final achieved pose of the action object at the terminal state is used for computing the evaluation metrics.
- **Trajectory Flow:** Using the same BC dataset with DAgger, we train a dense policy using PointNet++ [60] to predict a dense per-point 3D flow vector at each time step instead of a single 6-DOF transformation. Given this dense per-point flow, we add the per-point flow to each point of the current time-step’s point cloud, and we are able to extract a rigid transformation between the current point cloud and the point cloud transformed by adding per-point flow vectors using SVD, yielding the next pose. The final achieved pose of the action object at the terminal state is used for computing the evaluation metrics.
- **Goal Flow:** Instead of training a multi-step policy to reach the goal, we train a PointNet++ [60] network to output a single dense flow prediction which assigns a per-point 3D flow vector that points from each action object point from its starting pose directly to its corresponding goal location. Given this dense per-point flow, we add the per-point flow to each point of the start point cloud, and we are able to extract a rigid transformation between the start point cloud and the point cloud transformed by adding per-point flow vectors using SVD, yielding goal pose. We pass the start and goal pose into a motion planner (OMPL) and execute the planned trajectory. The final achieved pose of the action object at the terminal state is used for computing the evaluation metrics.

H Author Contributions

Chuer Pan designed and implemented the cross-correspondence TAX-Pose model, correspondence residuals, and the bi-directional weighted SVD method. She also designed, implemented, and conducted the simulation experiments of the NDF tasks as well as the study on varying the number of demos and the various ablation experiments. She also designed, implemented, and trained the models for mug hanging task in the real-world.

Brian Okorn proposed, designed, and implemented the cross-correspondence model, correspondence residuals, and the bi-directional weighted SVD method, as well as analyzed the invariances of the current framework.

Harry Zhang wrote early prototypes of TAX-Pose using residual flows without cross-attention, which later became a baseline of TAX-Pose. He also wrote the infrastructure of the PartNet-Mobility object placement task’s simulated data collection and training. He also wrote all the baselines in the PartNet-Mobility placement task. He designed and conducted all real-world robot experiments for both tasks in the real-world.

Ben Eisner designed the PartNet-Mobility tasks, implemented the Pybullet physics environment required for their rendering and simulation, and conducted training and evaluation of TAX-Pose on the PartNet-Mobility dataset. He also designed and evaluated the goal-conditioned variant of TAX-Pose.